Mapping long-term changes in inputs to the ventral tegmental area after a single drug exposure

Katrina Bartas[1], May Hui[2], Pieter Derdeyn[1], Kevin T. Beier[2-6]

1 Program in Mathematical, Computational, and Systems Biology. University of California, Irvine, Irvine, CA, USA 92697-4560
2 Department of Physiology and Biophysics, University of California, Irvine, Irvine, CA, USA 92697-4560
3 Department of Neurobiology and Behavior, University of California, Irvine, Irvine, CA, USA 92697-4560
4 Department of Biomedical Engineering, University of California, Irvine, Irvine, CA, USA 92697-4560
5 Department of Pharmaceutical Sciences, University of California, Irvine, Irvine, CA, USA 92697-4560
6 Center for the Neurobiology of Learning and Memory, University of California, Irvine, Irvine, CA, USA 92697

*Corresponding author
Contact information:
Kevin Beier
825 Health Sciences Road
Medical Sciences D337
Irvine, CA 92697
Phone: 949-824-1083
Email: kbeier@uci.edu

ABSTRACT:

Exposure to drugs of abuse causes long-lasting changes in connectivity to ventral tegmental area dopamine cells that contribute to drug-induced behavioral adaptations. However, it is not known which inputs are altered, largely due to technological limitations of previous methods. Here we used a rabies virus-based mapping strategy to quantify rabies-labeled inputs to ventral tegmental area cells after a single exposure to one of a variety of abused drugs – cocaine, amphetamine, methamphetamine, morphine, and nicotine – and compared the relative global input labeling across conditions using dimensionality reduction approaches. We observed that all tested drugs of abuse elicited input changes onto dopamine cells, in particular those projecting to the lateral shell of the nucleus accumbens and amygdala, and that these changes were common to all drugs tested. Interestingly, we also noticed that animals anesthetized with a ketamine/xylazine mixture exhibit a different brain-wide input pattern from those anesthetized with isoflurane, indicating that the method of anesthesia can influence rabies input labeling by inducing long-lasting changes in circuit connectivity. In addition, many input changes were common between animals anesthetized with ketamine/xylazine and those anesthetized with isoflurane but also given a single dose of a drug of abuse, suggesting that the ketamine/xylazine mixture can induce these long-lasting input changes. We found that many of the brain regions that exhibited changes in rabies input labeling in drug- vs. saline-treated mice were preferentially interconnected, and that select communities of brain regions showed similar changes for both drugs of abuse and ketamine/xylazine anesthesia. Lastly, the basal expression patterns of several gene classes were highly correlated with the extent of both addictive drug- or ketamine/xylazine-induced input changes, especially calcium channels. These results indicate that the expression of calcium channels is related to whether these inputs to dopamine cells are altered by drug exposure. Furthermore, ketamine/xylazine anesthesia induces a similar but different set of long-lasting input changes onto midbrain dopamine cells, indicating that caution should be taken when using ketamine/xylazine-based anesthesia in rodents when assessing motivated behaviors.

INTRODUCTION:

The ventral tegmental area (VTA) contains dopamine cells (VTA^{DA}) that play key roles in several behavioral processes, including reward, aversion, and motor control [1–3]. VTA^{DA} cells are heterogeneous, with recent studies identifying subpopulations of VTA^{DA} cells that differentially contribute to adaptive and pathological behaviors [4–7]. Numerous studies have mapped the input-output architecture of VTA cells generally, as well as subpopulations of constituent DAergic, GABAergic, and glutamatergic cells [7–12]. These studies have helped us to understand the biased input and discrete output logic of the VTA, as well as generate hypotheses regarding the function of circuits including the VTA.

In addition to normal adaptive behaviors, VTA^{DA} cells critically contribute to a variety of behaviors related to substance use disorder (SUD), including reward, sensitization, and withdrawal elicited by drugs of abuse [13–18]. For a variety of drugs of abuse, even a single exposure triggers long-lasting changes in synaptic plasticity onto VTA^{DA} cells [19,20]. Electrophysiological experiments revealed that drugs induce a long-lasting enhancement of excitatory synaptic strength onto VTA^{DA} cells [20]. Later, it was shown that inhibitory synaptic plasticity occurs in the VTA as well [21,22]. These changes have been shown to be essential for a variety of drug-induced behaviors, demonstrating their importance for triggering brain-wide circuit and synaptic adaptations [22–24]. Furthermore, the changes in excitatory synaptic plasticity specifically occur onto some cell types and not others [5], indicating that these adaptations are likely cell-type and pathway-specific. However, it remains unknown which sets of inputs are modified, and if these changes are consistent across abused drugs. Beyond synaptic plasticity, even less is known about how other forms of experience-dependent changes, including elevations in input activity, may contribute to addiction-related behaviors.

We recently showed that a single dose of cocaine causes long-lasting changes in cellular activity in inputs to VTA^{DA} cells [15,16]. These changes occur from the globus pallidus external segment (GPe) and bed nucleus of the stria terminalis (BNST) projections to the VTA that contribute to drug-induced reward and sensitization, or withdrawal anxiety, respectively [15,16]. Notably, while these studies focused on inputs from the GPe and BNST, the viral mapping results also demonstrated the existence of other input changes to the VTA that were not pursued in those studies. These unexplored connections may provide critical information about how drugs alter connectivity onto VTA^{DA} cells, which in turn contributes to drug-induced behavioral changes.

In this study, we explore the brain-wide changes elicited by a variety of different drugs, including drugs of abuse, an anesthetic mixture of ketamine/xylazine (K/X), or fluoxetine, a psychoactive but non-abused control substance. We find that K/X anesthesia alters the global set of rabies virus (RABV)-labeled inputs to VTA^{DA} neurons relative to isoflurane-anesthetized controls. We also find that K/X anesthesia induces overlapping input changes with the psychostimulants cocaine, amphetamine, and methamphetamine, as well as morphine, and nicotine. Lastly, we explore how basal gene expression patterns throughout the brain relate to connectivity changes induced by different drugs. Our study provides a first-of-its-kind exploration into how even a single drug exposure can change brain-wide connectivity patterns, as well as highlights some concerns about the potential effects of K/X anesthesia on motivated behavior.

MATERIALS AND METHODS:

Experimental Procedures

Animals: Mice were housed on a 12-hour light–dark cycle with food and water ad libitum. Males and females from a C57/BL6 background were used for all experiments in approximately equal proportions. Mice were approximately 3-4 months of age at the time of experiments. All surgeries were done under isoflurane or ketamine/xylazine anesthesia. All procedures complied with the animal care standards set forth by the National Institute of Health and were approved by the University of California, Irvine's Institutional Animal Care and Use Committee (IACUC).

Stereotaxic surgery: Mice were anesthetized with 3-4% isoflurane and maintained during surgery at 1-1.5% isoflurane, or with a mixture of ketamine (100 mg/mL) and xylazine (5 mg/mL). Mice were secured in a stereotaxic apparatus (Stoelting). Under aseptic conditions, guide holes were drilled and viruses were infused into the target sites using a glass capillary attached to a microinjection pump (WPI, UMP3T). 100 nL of AAVs or 500 nL of EnvA-pseudotyped RABV were infused at a rate of 1.6 nL/s. The glass capillary remained in place for 5 min following the infusion to allow for virus diffusion. After infusion, the surgical incision sites were closed with either sutures or Vetbond tissue adhesive (Patterson Veterinary). Vetameg (flunixin, Patterson veterinary) was administered for pain management and topical bacitracin was applied to prevent infection at the incision site.

For viral injections, for mapping experiments from a defined cell type, 100 nL of a 1:1 volume mixture of AAV-CAG-FLEx^{loxP}-TCB and AAV-CAG-FLEx^{loxP}-RABV-G was injected into the VTA of DAT-Cre [25], GAD2-Cre [26], or vGluT2-Cre mice [27]. Thirteen days later, animals were given

a single injection of a drug of abuse, fluoxetine, or saline. The following day, EnvA-pseudotyped RABV was injected into the VTA. Animals were sacrificed the following day. For cTRIO experiments shown in Figure 3, during the first surgery, AAV-CAG-FLEx^{FRT}-TCB and AAV-CAG-FLEx^{FRT}-RABV-G were injected into the VTA, and CAV2-FLEx^{loxP}-Flp was injected into an output site (NAcLat, amygdala, NAcMed, mPFC) during the same surgery. All other procedures were the same as above. RABV-labeled cells throughout the brain were manually quantified, as done previously [7,10,15].

Drug administration: Cocaine was administered (intraperitoneal injections) at a dose of 15 mg/kg, morphine at 10 mg/kg, methamphetamine at 2 mg/kg, amphetamine at 10 mg/kg, nicotine at 0.5 mg/kg, or fluoxetine at 10 mg/kg.

Dimensionality reduction of RABV input data

To visualize RABV counts data, we used Principal Component Analysis (PCA) and Uniform Manifold Approximation and Projection (UMAP). For our RABV input mapping experiments, cells were binned into 22 input regions: Cortex (anterior cortex), NAcMed, NAcLat, NAcCore, DStr, VP, PO, Septum, BNST, EAM, EP, GPe, PVH, LHb, MHb, CeA, LH, ZI, DR, LDT, PBN, and DCN. Altogether, this dataset consists of the input cell counts for these 22 regions across 122 mouse brains, with n=4 or 5 for each condition.

RABV input tracing data were reported as the percentage of total quantified labeled RABV inputs, as reported previously [7,10]. These data were further scaled using Z-score normalization. PCA was then implemented on these normalized data using the scikit learn library in Python with default parameters [28]. Weights for PCA models were visualized as heatmaps, reflecting the contribution of each feature to each principal component. UMAP was implemented using the UMAP library in Python [29]. To choose and standardize our UMAP parameters across analyses, we investigated which methods placed mouse brains of the same type and treatment close together most consistently. For the distance metric parameter, the metrics we found to perform best were Euclidean and cosine, but we chose to use the Euclidean metric for consistency with previous analyses [30]. For the number of neighbors parameter we chose a large number, ⅓ the size of each of our datasets, for a more global view of the data. Other parameters were kept at the default values. To account for the stochasticity of individual embeddings, we applied UMAP 20 times to each data set and found the results to be very similar, as found in previous analyses [30]. Clustered heatmaps and plots of these data were made using a combination of the Python

packages seaborn [31] and matplotlib [32]. The seaborn clustermap function was implemented with default values, including Euclidean distance as the distance metric.

To better visualize the distribution of a given condition in PCA and UMAP space, we overlaid the points with ellipsoids. Ellipsoids were centered at the average coordinate of a condition and stretched one standard deviation along the primary and secondary axes.

Brain Region Selection in the Allen Mouse Brain Atlas

To compare our data with connectivity data from the Allen Institute, we converted our 22 brain regions into regions or groups of regions defined by the Allen Atlas. This was necessary as our region annotations defined while doing cell counts of the RABV data were at times different from the Allen Mouse Brain Atlas-defined regions. 22 brain regions were used for RABV analyses but these were reduced to 20 brain regions (NAcMed, NAcLat, and NAcCore were merged into the NAc) for comparison with Allen Atlas data. In several cases, multiple Allen-defined regions were used to constitute a single region that we defined, as in the case of the cortex. A summary of these conversions is as follows:

Full brain region name	Standard abbreviation	Allen abbreviations
Cortex	Anterior cortex	PL ILA, ORB, GU, AI, MOs, MOp
Nucleus accumbens (medial)	NAcMed	ACB
Nucleus accumbens (lateral)	NAcLat	ACB
Nucleus accumbens (core)	NAcCore	ACB
Dorsal striatum	DStr	STRd
Ventral pallidum	VP	PALv
Preoptic area	PO	MPO, LPO
Septum	Septum	LSX, MS
Bed nucleus of the stria terminalis	BNST	BST
Extended amygdala area	EAM	MEA, AAA, NLOT, COA, MA, BMA, EPv, NDB
Internal Globus Pallidus	EP	GPi

External Globus Pallidus	GPe	GPe
Paraventricular nucleus of the hypothalamus	PVH	PVH
Lateral habenula	LHb	LH
Medial habenula	MHb	MH
Central nucleus of the amygdala	CeA	CEA
Lateral hypothalamus	LH	LHA
Zona incerta	ZI	ZI
Dorsal raphe nucleus	DR	DR, PAG
Laterodorsal tegmental nucleus	LDT	LDT
Parabrachial nucleus	PBN	PB
Deep cerebellar nuclei	DCN	CBN

Allen Mouse Brain Connectivity Atlas projection portrait construction

Projection portraits of the VTA were made using data from the Allen Mouse Brain Connectivity Atlas [33], and as described previously [30]. Briefly, data from 20 input brain regions, as defined in the above table, were downloaded and used for analyses. Experiments representative of each brain region were chosen for visualization. Connectivity of brain regions of interest to the VTA was visualized by showing a representative slice of the VTA and coloring the image based on high or low connectivity according to averaged AAV tracing data. AAV tracing data was averaged across experiments and across brain regions that grouped together according to weights assigned by PCA, as shown in Figures 1, 2, and 3, or by differences in RABV data between drugs and control treatment, as shown in Figure 4.

Data for projection portraits and for subsequent network construction was accessed using the python Allen SDK package, developed and maintained by the Allen Institute for Brain Science.

Allen Mouse Brain Connectivity Atlas connectivity network construction

In order to construct connectivity networks of defined VTA input sites, we again utilized the AAV projection data from the Allen Mouse Brain Connectivity Atlas [33]. The projection density of each region to others was normalized by the AAV injection volume, and then multiplied by the size (in

voxels) of the injected structure. These quantities were used to build a connectivity matrix, encoding the connectivity of each region with each of the others. We constructed and visualized connectivity networks using the python package Networkx, as shown in Figure 5. Nodes were spatially embedded using NetworkX's spring layout, placing brain regions with higher connectivity closer to each other.

To further visualize interconnectivity among the brain regions in this network, we used the Louvain method to detect communities [34]. Four distinct communities of brain regions were detected, as visualized in Figure 5.

Gene Expression Data Access and Processing

Gene expression data was downloaded from the Allen Institute's Anatomic Gene Expression Atlas (AGEA) [35], an in situ hybridization dataset which has annotated expression of 19,932 genes to every brain region defined in the Allen Mouse Brain Atlas. We used code written by Eli Cornblath (https://github.com/ejcorn/mouse_abi_tool) to access and download gene expression data for our regions of interest, as done in previous work [36]. To ensure only high quality data were included in our analyses, we filtered experiments based on metrics used in previous analyses of this dataset [37]. We retained genes for which there were data from coronal sections, or where the Pearson correlation coefficient across experiments was over 0.5 for a particular gene in our regions of interest. This filtering left us with 4,283 unique genes for the 36 Allen-defined brain regions to be aggregated to compare to our 22 quantified input sites from the RABV mapping data. We averaged data among brain regions that were defined differently in the atlas versus our RABV quantifications, which resulted in a total of 20 brain regions for comparative analyses, as detailed above. Data were normalized using a scaled sigmoid function, a method that is robust to outliers and was used in previous analyses of these data [56].

Gene expression data analysis and comparison to RABV data

To investigate how basal gene expression might be correlated to connectivity changes after drug exposure, we used processed data from the AGEA. To compare RABV data to the gene expression data, we presented the RABV data as either the ratio or the difference across two conditions. For each drug, or experimental condition, the RABV data for the drug were compared to the isoflurane controls. For the ratio, as used in Figures 7, and 8, we calculated the average RABV counts in each brain region for the experimental condition divided by the average RABV counts in each brain region for the isoflurane (control) condition. This resulted in a vector of 22

ratios for each drug comparison, one ratio for each brain region. For the difference, as used in Figure 6, we calculated the average RABV counts in each brain region for the drug condition minus the average RABV counts in each brain region for the isoflurane (control) condition. This resulted in a vector of 22 differences for each drug comparison, one difference for each brain region.

We first calculated the correlation of our differences between each drug and the control to gene expression data for each region. The Spearman correlation coefficient between the gene expression across regions to our RABV differences was used because the correlative relationship between these values cannot be assumed to be linear. A similar method was used in previous analyses [37]. A high positive correlation between a gene and an experimental condition ratio was interpreted as a greater susceptibility of a brain region to exhibit RABV labeling changes after drug exposure if this gene is highly expressed before drug exposure. A negative correlation between a gene and an experimental condition ratio was taken to mean this region would be more susceptible to RABV labeling changes after drug exposure if the gene expression level is low.

We performed GO analysis on the top 50 most highly correlated genes and also on the top 50 most negatively correlated genes. GO analysis was done using the EnrichR package [38]. Lists of genes with highly positive or negative correlations to our condition differences were compared to GO annotations using the coding language R. The 2021 version of two databases were queried: GO Biological Process and GO Molecular Function. GO enrichment analysis results were visualized in dot plots using the package ggplot2, as shown in Figure 6.

We next compared the drug/isoflurane ratios for a group of addictive drugs to gene expression of subsets of genes of interest (**Figure 7, 8**). Similar analyses were done for ketamine and fluoxetine (**Figure S8, S9**). The subgroups of genes used were synapse-related genes [39], ion-channel related genes [40], neurotransmitter receptor-related genes [41], differentially expressed genes related to substance dependence GWAS [42], and exo- and endocytosis-related genes [43]. Other subsets of genes of interest were defined using the Guide to Pharmacology database [44]. Correlation coefficients and p-values are reported in the figures.

RESULTS:

Dimensionality reduction methods identify differences in inputs of VTA cell populations

We and others previously showed that inputs to DAergic, GABAergic, and glutamatergic cells in the VTA receive inputs from similar brain regions, with some quantitative differences that varied depending on the study [10,12]. In our work we showed that connectivity differences in the VTA are largely a consequence of spatial organization of cells within the VTA [7,10,30]. The fact that the distributions of these three VTA cell populations are largely spatially overlapping may explain why the global inputs to each population are similar. However, one limitation in interpreting these studies is that they focused on individual comparisons of input counts on a per region basis. While this is a common approach in analyzing viral tracing data, and useful for both hypothesis generation and testing, it fails to account for the higher level organization of input patterns. When performing analysis of RABV tracing data, how can we go beyond considering single brain regions and better understand the wholistic change in connectivity? We recently used dimensional reduction approaches like principal component analysis (PCA) and uniform manifold approximation and projection (UMAP) to discover several modules of inputs to the VTA with similar variations and spatial projections [30], techniques which we applied further here.

Our first goal was to explore the potential differences in input patterns generated using RABV tracing to each of the DAergic, GABAergic, and glutamatergic neuron populations in the VTA using PCA. Doing so resulted in the three cell populations clustering into largely distinct groups (**Figure 1A**). We considered the first two principal components (PCs), which explain the most variance in the data. In PC space, DAT-Cre brains were characterized by low PC1 and low PC2 values, GAD2-Cre brains by high PC1 and low PC2 values, and vGluT2-Cre brains by high PC2 values. A significant advantage of PCA over other dimensionality reduction approaches is that because it is a linear approach, the weights of each feature's contribution to each PC can be clearly interpreted. In our case, we can infer which brain regions contribute most to the positive and negative dimensions of each PC. For example, in our data, DAT-Cre and GAD2-Cre brains were separated along PC1. Brain regions that contributed to the positive dimension of PC1 were the BNST, entopeduncular nucleus (EP), GPe, central amygdala (CeA), and zona incerta (ZI) (**Figure 1G**). These inputs were enriched onto GABAergic cells relative to DA cells. In order to identify where in the VTA these populations projected, we assembled projection portraits of these inputs to the VTA as we did previously [30]. This approach uses axonal projection data available from the Allen Mouse Brain Connectivity Atlas [33]. We first selected experiments where GFP was expressed in the regions of interest. Pixel values representing projection density were pulled from a representative coronal slice containing the VTA for each region. For a given set of inputs of interest, we averaged together their projections to the VTA to see if the group had any common

spatial trends (**Figure 1B**). The projection portrait of the positive PC1 inputs indicated that they preferentially project dorsally to areas surrounding the VTA (**Figure 1C**). In contrast, the regions that contributed most strongly to the negative dimension of PC1 were the anterior cortex, nucleus accumbens medial shell (NAcMed), ventral pallidum (VP), preoptic area (PO), septum, lateral habenula (LHb), medial habenula (MHb), and lateral hypothalamus (LH). These inputs were more highly labeled in DAT-Cre mice. The projection portrait of these inputs highlights the whole VTA and not surrounding regions (**Figure 1D**). While the distribution of starter cells in the VTA in DAT-Cre and GAD2-Cre mice is spatially overlapping [7], this analysis indicates that inputs with biases onto DA cells target the VTA itself while those biased onto GABAergic cells preferentially target areas dorsal and lateral to the VTA.

While DAT-Cre and GAD2-Cre conditions were separated along PC1, DAT-Cre and vGluT2-Cre conditions were separated along PC2. Regions that contributed to the positive dimension of PC2 included the LHb, MHb, EP, ZI, and deep cerebellar nuclei (DCN) as well as the cortex, while those contributing to the negative dimension included the NAcMed, nucleus accumbens lateral shell (NAcLat), nucleus accumbens core (NAcCore), dorsal striatum (DStr), and GPe (**Figure 1E-G**). The MHb and LHb both project medially in the VTA, whereas the NAcMed, NAcLat, NAcCore, DStr, and GPe all project laterally [30]. The projection portrait corresponding to the positive dimension of PC2 highlights the area dorsal of the VTA, as well as the medial aspect of the VTA (**Figure 1E**), while those corresponding to the negative dimension highlight the ventrolateral aspect of the ventral midbrain, including the substantia nigra pars reticulata (SNr) (**Figure 1F**). These results are consistent with the medial-lateral projection gradient that principally divides the projections into the VTA, with inputs from the basal ganglia projecting to the lateral portion of the VTA and the habenula projecting to the medial portion. As inputs from the MHb and LHb contribute positive weights to the PC2 axis and vGluT2-Cre brains are located on the positive end of the axis, it suggests that a majority of the vGluT2-expressing cells in the VTA are located within the medial portion of the VTA. This is consistent with previous reports using immunohistochemistry and in situ hybridization [45,46]. In addition, the EP, ZI, and DCN all project predominantly to the red nucleus, and the cortex also innervates the red nucleus, which contains glutamatergic neurons and is located dorsally to the VTA (**Figure 1E**). While injections for our viral mapping studies targeted the VTA and the vast majority of starter neurons were within the VTA, there were some starter neurons in vGluT2-Cre brains located in the red nucleus. In contrast, this was not the case in DAT-Cre brains [10]. As these starter populations were also largely spatially overlapping, the data indicate that inputs with biases onto glutamatergic cells target the

dorsomedial aspect of the VTA, while those with a relative bias onto DA cells preferentially target the ventrolateral aspect of the VTA.

While PCA is particularly useful due to the interpretability of the weights of the PCs, it does not allow for representation of non-linear relationships in high-dimensional data. To examine the overall relationship of input patterns between DAT-Cre, GAD2-Cre, and vGluT2-Cre cell populations, we performed a second analysis on inputs from each population using UMAP, which can capture more complex relationships than PCA. We found that DAT-Cre and GAD2-Cre brains were the most separated in UMAP space, with vGluT2-Cre brains located between them (**Figure 1H**). This is consistent with the overlap in neurotransmitters released by these cells; cells expressing DA markers such as tyrosine hydroxylase (TH) and traditional GABAergic markers such as GAD2 are nearly mutually exclusive, while there is considerable overlap between cells expressing DA markers and glutamatergic markers, as well as cells expressing GABAergic markers and glutamatergic markers [10,12,47–49]. Note that while DA neurons have been found to co-transmit DA and GABA [50,51], this occurs through a non-canonical GABA synthesis pathway, and therefore DA cells do not express typical markers of GABAergic cells, such as GAD2, used to define the Cre line in our study.

Since individual UMAP embeddings are stochastic depending on initial seeding conditions, we examined the average Euclidian distance between the same data points in 20 UMAP embeddings of the same data and plotted the averaged results as a correlogram. This showed that DAT-Cre and vGluT2-Cre brains were more similar to one another, and the GAD2-Cre brains were the most distinct from the other conditions (**Figure 1I**). These results are thus consistent with the known neurochemical overlap between these cells, and indicate that DAT-Cre and vGluT2-Cre label more overlapping cells with each other than with GAD2-Cre. Overall, these initial observations provide a validation of our approach for dissecting the relationships between input patterns and different cell types within the VTA, as the conclusions about the relationship between input regions and cell types are in agreement with other studies using different complementary methodologies.

A single injection of a variety of substances changes brain-wide input patterns to VTA cells

We previously showed that a single dose of cocaine caused a long-lasting elevation in labeling from inputs from the GPe onto VTA^{DA} cells [15]. This led us to explore the functional role of GPe inputs to the midbrain in the development of drug-induced behavioral changes, facilitating the

identification of the key role that parvalbumin cells in the GPe play in the development of cocaine-induced conditioned place preference and locomotor sensitization. Importantly, these data indicated that the input changes identified using RABV were functionally relevant. In that study, we found that labeled inputs from the GPe were elevated by all tested drugs of abuse but not by saline nor the psychoactive but non-addictive fluoxetine. We also identified several other differences in input labeling in addition to the changes in the GPe that we did not pursue further in that study, indicating that drugs of abuse likely broadly alter brain-wide input patterns beyond the GPe. Here, we wanted to ask two questions: 1) What are the brain-wide changes in input patterns to VTA^{DA} cells that result from an injection of one of a number of psychoactive substances, and 2) how do these potential drug-induced differences relate to differences between unique cell types in the VTA?

In order to explore these questions, we performed experiments with ten separate groups of mice; 2 groups of GAD2-Cre mice, and 8 groups of DAT-Cre mice. The GAD2-Cre mice were all anesthetized with isoflurane and administered either saline or cocaine. The DAT-Cre mice were given either isoflurane or K/X-based anesthesia. The K/X-anesthetized mice were administered saline. The isoflurane anesthetized mice were administered either saline, fluoxetine, amphetamine, cocaine, meth, morphine, or nicotine. RABV mapping was performed from targeted VTA cells in all cases, and the brain-wide inputs were quantified. We then performed PCA on these RABV tracing datasets. When comparing the input tracing patterns between mice, we found that brains from GAD2-Cre mice were located in the positive dimension of PC1, while those from DAT-Cre mice were located in the negative dimension (**Figure 2A**), regardless of the substance administered. The positive dimension of PC1 received contributions from largely the same sets of regions as in the previous analysis of DAT-Cre, GAD2-Cre, and vGluT2-Cre brains, which included the BNST, EP, ZI, CeA, as well as the DCN (**Figure 2B**). Given that the same set of brain regions differentiated DAT-Cre and GAD2-Cre brains along PC1 in both datasets, this suggests that the intrinsic differences in inputs to different cell populations in the VTA are more pronounced than differences induced by the injected substances. Notably, none of these patterns could be obtained by chance; scrambling the sample identity and percentage of RABV-labeled cells in each input site resulted in groups that overlapped in both PCA and UMAP space (**Figure S1**).

To specifically explore potential drug-induced differences in input labeling, we removed GAD2-Cre brains from the dataset and repeated the same analysis to focus only on data obtained from

DAT-Cre mice. When performing this analysis, PC1 and PC3 largely failed to differentiate the conditions, while PC2 differentiated the drugs of abuse from the controls (**Figure 2C-D**). The most negative weights to PC1 were contributed by the basal ganglia inputs that project to the SNr, located ventrolaterally to the VTA (**Figure 2E-F**) while positive contributors came from brain regions that projected more medially (LHb, MHb, dorsal raphe (DR)) and centrally to the VTA (ventral pallidum (VP), PO, extended amygdala area (EAM), paraventricular nucleus of the hypothalamus (PVH), and LH) (**Figure 2E, G**). This is consistent with a gradient along the medial-lateral axis [30]. As it did not differentiate the conditions, this axis likely represents experimental variations in the location of starter cell populations. The regions with the largest positive contribution to PC2 included the EAM, parabrachial nucleus (PBN), DR, EP, and LH, with lesser contributions from the GPe, DCN, ZI, CeA, and BNST (**Figure 2E, H**). Notably, this group contains brain regions that are involved in the brain's stress response and have been implicated in drug-induced behaviors [52,53]. For example, we recently showed the importance of the GPe in conditioned place preference and locomotor sensitization and the BNST in drug-induced withdrawal [15,54]. The regions with the largest negative contribution to PC2 included the NAcMed, NAcCore, DStr, Septum, and MHb (**Figure 2E, I**). These results together demonstrate that drugs of abuse cause long-lasting changes in input populations to DA cells, and that we can identify which sets of inputs distinguish drug-treated vs. control-treated brains. These changes may be functionally important, as we previously demonstrated the functional role of two inputs that we identified as differing between drug-treated and control conditions.

Lastly, we wanted to explore the overall relationship between input changes induced by different drugs. As before, we used UMAP to explore the higher-level organization of these conditions. We found that the saline-treated group overlapped with the fluoxetine-treated group but not the K/X-anesthetized group (**Figure 2J**). These conditions were segregated from animals treated with the drugs of abuse - psychostimulants, morphine, and nicotine. Our analysis of the relationships between individual conditions, generated using the Euclidian distances between points in 20 UMAP embeddings as before, demonstrated that the expected control conditions formed a cluster (saline, fluoxetine) distinct from the other groups. Interestingly, the K/X-anesthetized animals were more closely associated with the mice treated with addictive drugs, in particular morphine, than with controls (**Figure 2K**). This suggests that drugs of abuse cause similar changes in brain-wide input patterns to one another in DAT-Cre brains, and that input patterns in K/X-anesthetized animals more closely resemble morphine-treated mice than saline-treated mice. This indicates that the method of anesthesia, either using isoflurane or K/X, results in different patterns of input

labeling. Given the similarity of input patterns in K/X-anesthetized mice to isoflurane-anesthetized mice treated with a drug of abuse but not saline, we suspect that K/X-anesthesia triggers changes in input patterns in rodent brains that last at least the five day duration of these experiments.

Anesthetic doses of ketamine/xylazine cause long-lasting changes in inputs to VTA^{DA}→NAcLat and VTA^{DA}→amygdala cells

We noted in previous analyses that animals anesthetized with a K/X mixture did not completely associate with those anesthetized with isoflurane (**Figure 2**). When comparing only inputs of isoflurane-anesthetized animals to those of K/X-anesthetized animals using PCA, these conditions completely segregated (**Figure 3A**). This separation was driven by positive weights from the VP, PO, EAM, PVH, LH, and PBN along PC1, whose combined projection portrait broadly targets the VTA (**Figure 3A, J, O**), and the NAcLat, DStr, GPe, and PVH along PC2, whose combined projection portrait targets ventrolateral to the VTA (**Figure 3A, J, P**).

Next, we wanted to assess which DA cells in the VTA may be impacted by whether the animals received isoflurane or K/X-based anesthesia. We performed cell type-specific Tracing of the Relationship between Inputs and Outputs (cTRIO) for each of four different VTA^{DA} subpopulations: those projecting to the NAcMed, NAcLat, amygdala, or mPFC, and receiving either isoflurane or K/X-based anesthesia. The differences in input patterns were most pronounced for VTA^{DA}→NAcLat cells, where the isoflurane- and K/X-treated groups segregated completely, both in PCA and UMAP space (**Figure 3B-C**). Groups differed along both PC1 and PC2, with K/X-treated brains being characterized by lower PC1 values which received contributions principally from the anterior cortex, NAcMed, NAcLat, NAcCore, septum, PVH, and MHb, as well as higher PC2 values which received contributions from the VP, PO, EAM, LHb, and LH (**Figure 3B, K, Q, R**). Notably, K/X-treated mice and cocaine-treated mice completely segregate from one another in both PCA and UMAP space, indicating that the K/X-induced changes are distinct from those induced by cocaine (**Figure 3B-C**). The similarity in projection portraits for weights that contribute more to the K/X-treated group in VTA^{DA}→NAcLat (**Figure 3Q, R**) and all VTA^{DA} neurons (**Figure 3O, P**) is consistent with the observation that VTA^{DA}→NAcLat neurons comprise the majority of VTA^{DA} neurons, as noted in previous studies [7,10]

In addition to VTA^{DA}→NAcLat cells, we observed some segregation of isoflurane and K/X-treated conditions in VTA^{DA}→amygdala cells, which was more apparent in UMAP space than PCA (**Figure 3D-E**). The lack of clear differentiation in PCA space makes it difficult to interpret which

input sites may be contributing to the differentiation in conditions that we observe (**Figure 3D, L**). In the VTA^{DA}→NAcMed and VTA^{DA}→mPFC subpopulations, the separation between isoflurane and K/X-treated conditions was much less pronounced (**Figure 3F-I**), and unlikely to be significant, as similar separations were observed by chance (**Figure S2**). Notably, when considering inputs to all VTA^{DA} cells, the projection portraits that indicate the inputs most highly elevated or depressed in K/X-treated mice highlight either the entire VTA, or the ventrolateral aspect of the VTA (**Figure 3O, P**). These projections are consistent with the locations of the VTA^{DA}-amygdala and VTA^{DA}→NAcLat cells, respectively. In contrast, the portraits do not highlight the medial or ventromedial aspects of the VTA, which is the location of VTA^{DA}→mPFC and VTA^{DA}→NAcMed cells [30,55], indicating that K/X anesthesia impacts inputs that preferentially target VTA^{DA}-amygdala and VTA^{DA}→NAcLat cells.

Comparison of input pattern differences induced by different drugs

Our results so far indicate that injections of anesthetic doses of K/X cause brain-wide changes that differ from both isoflurane-anesthetized saline-treated animals as well as those injected with psychostimulants, morphine, or nicotine (**Figures 2-3**). To further explore the nature of the drug-induced changes, we explored which areas of the VTA could be impacted by input changes induced by exposure to each drug. We accomplished this by producing VTA projection portraits for each drug. These portraits were created by weighting the input projections according to the relative enhancement of RABV labeling of inputs relative to isoflurane/saline controls for ratios over a threshold over 1.5 (**Figure 4**). This approach allowed us to examine if the brain regions that showed elevated input labeling following administration of a substance innervated any particular regions of the VTA [30]. This information can then be used to infer which VTA cell populations may be preferentially influenced by each drug [30].

We first evaluated the projection portrait of regions influenced by a single injection of the control fluoxetine relative to the control saline-injected condition. Fluoxetine mildly altered the projection portrait, most notably in the ventromedial aspect of the VTA (**Figure 4A**). This is where VTA^{DA}→NAcMed and VTA^{DA}→mPFC neurons are located [30,55]. K/X anesthesia yielded a similar projection portrait to fluoxetine, though the area covering the VTA as well as that immediately lateral to the VTA were more prominent than in the control fluoxetine group (**Figure 4B-C**). This suggests that the input changes following K/X anesthesia were more widespread than changes following fluoxetine. The area covering the center of the VTA as well as the lateral VTA reflects the positions of VTA^{DA}→amygdala and VTA^{DA}→NAcLat cells, respectively [7,55]. Thus,

this result is consistent with the segregation of isoflurane- and K/X-anesthetized conditions in the VTA^{DA}→NAcLat and VTA^{DA}→amygdala cTRIO conditions (**Figure 3B-E**). In contrast to K/X anesthesia, psychostimulants, morphine, and nicotine each produced similar projection portraits with prominent innervation of the SNr (**Figure 4D, S3**). This projection portrait is produced by large contributions from inputs in the basal ganglia [30]. We conclude that a common feature of psychostimulants, morphine, and nicotine is the elevation of input labeling from several basal ganglia structures that project to the SNr, which does not occur in K/X-anesthetized mice (**Figure 4E**). Rather K/X anesthesia elevates labeling predominately in inputs that project directly to the VTA.

Ketamine/xylazine anesthesia triggers input changes in distinct brain modules

Each of the projection portraits that we have generated are based on RABV mapping data from VTA^{DA} cells. Specifically, the portraits display projections from input sites that provide a relatively higher fractional contribution to VTA^{DA} cells in a certain experimental condition relative to a control. Thus, these portraits do not provide information about potential interconnectivity of the 22 input nodes that we are studying. While our RABV mapping data do not indicate whether the same cells that provide input to VTA^{DA} cells are the same as those connecting to other brain regions, if regions that show coordinated changes in RABV-labeling are preferentially interconnected, it might indicate coordinated changes amongst interconnected modules within the brain. Supporting this hypothesis are previous studies showing that the basal ganglia, from which we often observe multiple input changes or none, is heavily interconnected and can be considered a functional module [56,57]. In order to explore this possibility, we again used projection data from the Allen Mouse Brain Connectivity Atlas. To assess the interconnectivity of VTA inputs, we quantified projections from each VTA input site to each of the other input sites and built a network representation. In this network, nodes represent individual brain regions and edges represent projections between them. These edges are weighted according to the strength of that connection relative to the size of the source region. With these networks, we used the Louvain community detection algorithm to detect local groups of nodes that are more connected with each other than with other nodes on the network. This analysis demonstrated the existence of four distinct communities that can largely be classified as 1) cortical (yellow), 2) basal ganglia, (green) 3) extended amygdala/basal forebrain and parabrachial nucleus (blue), 4) everything else (purple) (**Figure 5**).

To assess how these communities of inputs are changed for each experimental condition, we generated network visualizations incorporating the ratio of RABV-labeled inputs relative to isoflurane/saline mice as the size of nodes. We observed that fluoxetine treatment resulted in only minor elevations in several inputs in community 4, including the PVH, LH, and PAG/DR (**Figure 5A**). In contrast, K/X anesthesia induced elevated labeling in the majority of brain regions in community 3, with several increases in community 4 and none in 1 or 2 (**Figure 5B**). This indicates that K/X anesthesia induced multiple changes in inputs within select communities and not others. In contrast, psychostimulants, morphine, and nicotine elevated input labeling in similar brain regions in community 3, more in community 4, and several within community 2, most notably the GPe and EP (**Figure 5C**). This pattern was observed in the drug condition as a whole as well as each drug individually (**Figure S4**). The elevation in labeling in several regions of the basal ganglia network is consistent with the results using the projection portraits in the VTA and suggests that the primary difference between psychostimulants, morphine, and nicotine relative to anesthetic doses of K/X is that the former enhance the connectivity from a broader array of input sites, principally several nodes in the basal ganglia including the GPe and EP.

Exploring gene expression patterns that predict changes in RABV input labeling

Our data indicate that changes in RABV-labeled input patterns induced by particular drugs of abuse tend to occur within particular communities, and the identity of those communities depends on the type of substance being administered. We next wanted to explore if these patterns of input labeling might be related to particular gene expression profiles present at the input sites. This approach may provide information about how basal gene expression profiles influence changes in connectivity to VTA^{DA} cells after the administration of various drugs. To do this, we calculated the correlation of gene expression data from the Allen Gene Expression Atlas (AGEA) to the difference between inputs labeled in each region in experimental conditions and isoflurane/saline-treated controls. After filtering AGEA data for only high-quality experiments, we were left with 4,283 genes to which we could calculate correlations within our 22 input brain regions of interest.

We first identified genes or pathways that may be linked to elevations or depressions in RABV labeling for each condition. To do this, we selected genes that were highly positively or negatively correlated to differences between isoflurane anesthetized, saline-treated controls and isoflurane-anesthetized animals treated with a single dose of a psychostimulant, morphine, nicotine, or fluoxetine, or K/X anesthetized mice. We used the top 50 genes that were either positively or negatively correlated and performed gene ontology (GO) analyses. Starting with drugs of abuse,

the positively correlated genes were most significantly associated with inhibitory ligand-gated chloride channels as well as endo/exocytic membranes and synaptic vesicles (**Figure 6A**), suggesting that higher basal expression of these genes may be related to larger changes in connectivity induced by drugs of abuse. Conversely, there were many more genes that were negatively correlated to drug-induced changes in RABV labeling. The most negatively correlated genes were most closely associated with negative regulation of long-term synaptic potentiation (**Figure 6B**), suggesting that regulation of synaptic plasticity in input cell populations may be a key indicator of susceptibility to drug-induced differences in RABV input labeling. In addition, other interesting classes of genes that are negatively associated with drug-induced changes in RABV labeling include regulation of synapse structural plasticity, regulation of calcium ion transport, cellular response to Ca^{2+} ions, and regulation of potassium ion transporters (**Figure S5**), which relate to synaptic and cellular processes of plasticity and intrinsic excitability, while those that were positively correlated include anion channels and syntaxin binding (**Figure S6**).

We also explored which gene expression patterns may be related to input changes driven by K/X anesthesia. Anion channel activity, particularly GABA receptor expression, again shows up as one of the most significant positive associations (**Figure 6C-D**), along with a variety of metabolic processes. Notably, these gene expression patterns were not correlated with input changes induced by fluoxetine (**Figure S7**). These results suggest that changes in RABV-labeled inputs induced by drugs of abuse are positively correlated to the basal expression of genes related to inhibitory synaptic transmission as well as synaptic plasticity and negatively associated with expression levels of genes associated with Ca^{2+} and K^{+} ions.

GO analysis provides a useful overview of the broad classes of genes that are represented as the most highly correlated to differences between two conditions. To further assess which classes of genes are the most closely related to the differences in drug-evoked RABV labeling relative to controls, we performed linear regressions of the ratios of RABV labeling in experimental vs. control conditions relative to the mean of RNA *in situ* hybridization data for a particular class of genes. We observed an overall significant and slightly negative correlation between the RABV labeling ratio and the gene expression mean ($p = 2.1 \times 10^{-3}$) for all 4,283 genes (**Figure 7A**). Among the gene expression classes that we examined, the most significant association was between RABV-labeled inputs and ion channel gene expression ($p = 1.3 \times 10^{-9}$; **Figure 7B**), consistent with our results from GO analyses. The next most significant classes were neurotransmitter receptors ($p = 1.9 \times 10^{-6}$) and synapses ($p = 1.6 \times 10^{-5}$), followed by genes that

have been linked to substance use disorders (SUDs) through Genome-Wide Association Studies (GWAS; $p = 7.7 \times 10^{-4}$) as well as endo/exocytosis genes ($p = 2.3 \times 10^{-3}$). Each of the above relationships showed a negative correlation of RABV ratios with gene expression. Each of these were likely meaningful, as the p-values were higher for the relationship between RABV labeling ratios and gene classes that are likely irrelevant to RABV labeling, such as mitochondrial genes ($p = 1.4 \times 10^{-2}$), sugar transporters $p = 1.0 \times 10^{-2}$), and tumor-associated genes ($p = 7.0 \times 10^{-2}$; **Figure 7G-I**).

As the class of ion channel genes was the most closely related to differences in RABV-labeled input patterns, we assessed which ion channels may be most closely linked to RABV labeling differences between conditions. The most significant relationship was between Ca^{2+} channel genes ($p = 4.4 \times 10^{-10}$), followed by Cl^- ($p = 6.1 \times 10^{-5}$), K^+ ($p = 2.9 \times 10^{-3}$), and Na^+ channels ($p = 0.30$; **Figure 8A-D**). The expression levels of these channels, in particular Ca^{2+} and K^+ channels may most closely be linked to regulating a variety of cellular processes, including immediate early gene expression networks as well as cellular excitability. Ligand-gated channels ($p = 4.1 \times 10^{-5}$) were more strongly related with RABV labeling than voltage-gated ion channels ($p = 7.4 \times 10^{-4}$) or other types of ion channels ($p = 0.21$; **Figure 8E-G**). Among the ligand-gated channels, the glutamate receptors were the most strongly linked ($p = 3.1 \times 10^{-7}$; **Figure 8H**). The next most strongly linked gene classes were acetylcholine receptors ($p = 2.4 \times 10^{-4}$), GABA receptors ($p = 1.8 \times 10^{-3}$), and glycine receptors ($p = 1.4 \times 10^{-3}$) (**Figure 8I-K**). Notably, glycine receptors were the only class of genes that we analyzed that were positively correlated with RABV labeling. Similar patterns were observed for K/X anesthetized mice (**Figure S8**), but not with isoflurane-anesthetized, fluoxetine-treated mice (**Figure S9**). These results together indicate that the basal expression levels of a variety of ion channels, particular Ca^{2+} and ligand-gated ion channels, are the most highly related to the RABV labeling ratio and thus, likely critical for driving elevations or depressions in RABV labeling following a single injection of a variety of drugs of abuse or K/X anesthesia.

DISCUSSION:

Here we explored the long-term consequences of a single injection of a variety of abused drugs on the connectivity of VTA^{DA} cells. We first confirmed that dimensionality reduction approaches could adequately differentiate the connectivity between different cell populations in the VTA, and showed which inputs differentiate DAergic, GABAergic, and glutamatergic cells in the VTA (**Figure 1**). We then showed that a variety of drugs of abuse as well as K/X-based

anesthesia trigger long-lasting changes in the brain-wide input patterns to VTA cells, which were clearly observable though less substantial than the differences in input connectivity to VTA^{DA} and VTA^{GABA} neurons (**Figure 2**). We used our cTRIO method to identify DA cell type-specific changes induced by cocaine as well as K/X anesthesia, implicating the VTA^{DA}→NAcLat and VTA^{DA}→amygdala cells as being the populations exhibiting the most substantial input changes (**Figure 3**). We then produced projection portraits of the most highly altered inputs in different experimental conditions and found that most inputs elevated in the K/X anesthesia condition targeted the VTA (**Figure 4B**), while inputs elevated by psychostimulants, morphine, and nicotine targeted the VTA as well as the adjacent SNr (**Figure 4D**). While input sites altered by K/X anesthesia largely resided within 2 connected communities (**Figure 5B**), the inputs altered by other drugs were more distributed and included the GPe and EP, which are in the basal ganglia (**Figure 5C**). We then explored intrinsic gene expression patterns throughout the brain that relate to the elevation or depression in RABV labeling by different drugs, finding that expression levels of ion channels, neurotransmitter receptors, and synapse-related genes were all significantly negatively correlated with RABV input labeling ratios (**Figure 7**). Among ion channels, Ca^{2+} channels and glutamate receptors were the most strongly linked with RABV labeling changes (**Figure 8A, H**). These results together indicate that a variety of different drugs of abuse trigger long-lasting input changes throughout the brain that demonstrate several characteristic patterns. They also indicate that K/X anesthesia induces a separate but related set of input adaptations to VTA^{DA} cells, providing a cautionary warning against using K/X anesthesia when assessing motivated behavior. Our findings will be discussed in further detail below.

Drugs of abuse induce changes in connectivity onto VTA^{DA} neurons from common and distributed input populations throughout the brain

We used PCA and UMAP to explore the relationship between brain-wide input patterns to different cell populations in the VTA, and in animals given a different drug treatment. We first found that we could differentiate the input patterns to different VTA cells using dimensionality reduction methods (**Figure 1**), and that these differences were larger than the differences in inputs from the same cell populations in animals given a drug of abuse vs. saline (**Figure 2A**). In addition, the input patterns to VTA^{DA} cells in animals treated with a single exposure to a drug of abuse segregated from those from control saline-treated animals and fluoxetine-treated animals (**Figure 2C**). Differences were apparent on the 2nd PC axis which was driven by positive weights from the GPe, EP, EAM, LH, ZI, DR, and PBN and negative weights from the NAcMed, NAcCore, DStr, Septum, and MHb (**Figure 2E**). This axis separated drug-treated and control animals, respectively.

We had previously explored the critical role of the GPe in cocaine-elicited locomotor sensitization as well as conditioned place preference [15]. We had also noted in that study that the EAM, EP, ZI, and MHb's inputs were significantly different between either cocaine vs. saline conditions or all drugs vs. saline conditions; these regions have generally been implicated in cocaine addiction [58–61]. While these drug-induced differences in input labeling were less substantial than intrinsic cell type connectivity differences (**Figure 2A**), both tend to be difficult to pull out from traditional bar graph-based approaches [7,12], yet are clearer when using dimensionality reduction methods such as PCA and UMAP. This larger difference in inputs between cell types than between animals receiving a control vs. single drug experience is perhaps not surprising, as different populations of cells may receive different sets of inputs from one another, and these are likely more stable across experiments than the differences in connectivity triggered following a single exposure to a drug of abuse.

The results in this study further confirm our previous observations that a single exposure to a variety of drugs of abuse triggers long-lasting changes in inputs to VTA^{DA} neurons. Our interpretation of these data is that the changes are largely being driven by a change in the activity of input cells, as we have shown twice using fiber photometry and slice electrophysiology [15,16]. However, we have not confirmed that changes in RABV labeling reflect persistent activity modifications in all identified input changes. For example, while it is intuitive that the efficiency of RABV labeling of an input site should scale with the number of synaptic connections, it has not been demonstrated to do so. Also, while RABV labeling has not been shown to detect a change in synapse strength, it may be able to detect them should they occur. As a single exposure to a variety of drugs of abuse alters the strength of both excitatory and inhibitory inputs in the VTA [5,20–22], we cannot rule out that changes in synapse number or strength may also influence the observed connectivity results.

Ketamine/xylazine anesthesia alters the input landscape of VTA^{DA} cells

We observed that animals anesthetized with a K/X mixture showed a different pattern of input labeling to VTA^{DA} cells than animals anesthetized with isoflurane. These data indicate that at least one of these methods of anesthesia alters brain-wide inputs to VTA^{DA} cells. While with current methods we cannot test what the input patterns are in the absence of anesthesia as doing so would be inhumane to the mice, we suspect that isoflurane anesthesia has minimal effect on the brain-wide inputs to VTA^{DA} cells. This is largely because animals treated with a drug of abuse with isoflurane anesthesia look more similar to those receiving saline and K/X anesthesia than to those receiving saline and isoflurane anesthesia. In addition, ketamine is a drug with known abuse

potential [62–65]. While the anesthetic doses used here (100 mg/kg) are well above the doses used recreationally (~1 mg/kg), the changes that we observed with K/X anesthesia may be related to the abuse potential of ketamine. Interestingly, we observed that the K/X-induced input changes were most similar to those induced by 10 mg/kg of morphine (**Figure 2K**). Recent studies have suggested that antidepressant doses of ketamine may work in part via the opioid system; indeed it has been known for some time that ketamine binds the mu opioid receptor [66–69], and it was more recently shown that the opioid antagonist naltrexone blocks the antidepressant effects of ketamine [70,71]. Given that anesthetic doses of ketamine (100 mg/kg) are roughly 10 times higher than antidepressant doses of ketamine (~10 mg/kg), K/X anesthesia almost certainly engages the opioid system.

Notably, while K/X anesthesia as well as psychostimulants, morphine and nicotine induced brain-wide changes in input labeling, the patterns of these changes were distinct. Projection portraits of K/X anesthesia mostly included inputs that project to the VTA itself, as well as towards the lateral aspect of the VTA, where the VTA^{DA}→amygdala and VTA^{DA}→NAcLat cells, respectively, are located. This is in contrast to psychostimulants, morphine and nicotine, which have a more distributed set of input changes that include an elevation of input labeling from the GPe and EP. Notably, these changes are quite consistent across drugs of abuse, providing further evidence that drugs of abuse with different mechanisms of action share a common set of circuit adaptations.

Relationship of gene expression with the extent of drug-induced RABV input labeling

In this study we observed correlations of gene expression patterns with the extent of elevations and depressions of RABV labeling induced by one of several drugs. We observed a slightly negative correlation of RABV labeling changes with the overall level of gene expression across the brain. We are not sure of the functional implications of this negative correlation, though it could point to the potential for an experience-induced elevation in gene expression levels that in turn could drive changes in RABV labeling; essentially, if initial gene expression levels are lower, it leaves a higher potential for experience-induced elevations. We observed highly significant negative correlations of RABV labeling changes induced by drugs of abuse with the levels of expression of ion channel genes, neurotransmitter receptor-related genes, and synapse-related genes. These results indicate that the expression levels of these genes could be used as predictive biomarkers of which regions are likely to undergo drug-induced changes in connectivity to VTA^{DA} cells. They also suggest that the expression levels of these gene classes are related to the drug-induced changes in RABV labeling. As the correlation is negative, it means that the less

these particular gene classes are expressed, the higher the elevation in drug-induced RABV input labeling. It may be that expression of any of these classes is inhibitory towards RABV transmission, and thus the reduced expression facilitates RABV infection. Alternatively, it could be that there is more potential for a drug-induced rise in gene expression level, and thus the change in expression level of these classes is what is driving changes in RABV labeling following drug exposure. To differentiate between these possibilities, further study is needed. For example, single cell RNA sequencing or quantitative PCR approaches could be used to assess the relative levels of gene expression in target regions following a drug exposure relative to controls. These studies would clarify the effects of a single drug exposure on the transcription of various gene classes and provide insight into how these gene classes may contribute to drug-related changes in brain connectivity.

Of particular interest to us is the strong and highly significant negative correlation between the extent of calcium ion channel expression and induction of changes in RABV labeling by drugs of abuse (**Figure 8A**). These results indicate that the lower basal expression of these channels, the higher the induction of RABV changes, which we believe points to a greater elevation of spontaneous activity in these input cells following drug exposure. Calcium channels have been implicated in substance abuse through Genome-Wide Association Studies (GWAS) [72], and molecules that target these channels have shown some promise as addiction therapeutics [73–78]. By showing that the basal expression levels of these genes in targeted brain regions is strongly related to the change in RABV input labeling, our data provide a link between expression of these channels and how they relate to drug-induced changes in brain connectivity. It is of particular interest that Ca^{2+} and not Cl^{-}, Na^{+}, or K^{+} channels are highly correlated to RABV input labeling changes. Ca^{2+} is critically involved as a second messenger in neurons that affects a variety of processes including transcription, transmission of the polarizing signal, and synaptic transmission, whereas the other ions are mostly involved only in facilitating or inhibiting formation and propagation of the action potential. Thus that levels of calcium channels are related to drug-induced input changes is consistent with the idea that neurons function as integrators, rather than simple conduits for information transfer, as these are the critical channels that relate to how experiences influence brain changes. However, further studies are needed to test these hypotheses. Understanding this relationship further will help to illuminate the relationship between basal gene expression levels, drug-induced changes in RABV labeling, and substance abuse, providing mechanistic insights into how inter-individual differences influence susceptibility to substance abuse.

ACKNOWLEDGEMENTS:
We would like to thanks Hemmings Wu and Zhoule Zhu for their thoughtful critique of our manuscript.

AUTHOR CONTRIBUTIONS: KTB performed the viral tracing experiments, KB performed the majority of computational analyses of the data, PD assisted with network constructions and projection portraits, MH assisted with figure preparation, and KB and KTB wrote the manuscript.

FUNDING: This work was supported by the NIH (R00 DA041445, DP2 AG067666, R01DA054374, R01DA056599, R01NS130044), Tobacco Related Disease Research Program (T31KT1437, T31P1426), American Parkinson Disease Association (APDA-5589562), Alzheimer's Association (AARG-NTF-20-685694), New Vision Research (CCAD2020-002), Brightfocus Foundation (A2022031S), and the Brain and Behavior Research Foundation (NARSAD 26845) to KTB, T31DT1729 to MH, T32 GM136624 to KB and PD, and NSF GRFP DGE-1839285 to PD.

COMPETING INTERESTS: The authors have nothing to disclose.

REFERENCES:

1. Bromberg-Martin ES, Matsumoto M, Hikosaka O. Dopamine in Motivational Control: Rewarding, Aversive, and Alerting. Neuron. 2010;68:815–834.
2. Lammel S, Lim BK, Malenka RC. Reward and aversion in a heterogeneous midbrain dopamine system. Neuropharmacology. 2014;76:351–359.
3. Wise RA. Dopamine, learning and motivation. Nat Rev Neurosci. 2004;5:483–494.
4. Kim CK, Yang SJ, Pichamoorthy N, Young NP, Kauvar I, Jennings JH, et al. Simultaneous fast measurement of circuit dynamics at multiple sites across the mammalian brain. Nat Methods. 2016;13:325–328.
5. Lammel S, Ion DI, Roeper J, Malenka RC. Report Projection-Specific Modulation of Dopamine Neuron Synapses by Aversive and Rewarding Stimuli. Neuron. 2011;70:855–862.
6. Lammel S, Lim BK, Ran C, Huang KW, Betley MJ, Tye KM, et al. Input-specific control of reward and aversion in the ventral tegmental area. Nature. 2012;491:212–217.
7. Beier KT, Steinberg EE, Deloach KE, Xie S, Miyamichi K, Schwarz L, et al. Circuit Architecture of VTA Dopamine Neurons Revealed by Systematic Input-Output Mapping. Cell. 2015;162:622–634.
8. Menegas W, Bergan JF, Ogawa SK, Isogai Y, Venkataraju KU, Osten P, et al. Dopamine

neurons projecting to the posterior striatum form an anatomically distinct subclass. Elife. 2015;4:1–30.

9. Watabe-Uchida M, Zhu L, Ogawa SK, Vamanrao A, Uchida N. Whole-Brain Mapping of Direct Inputs to Midbrain Dopamine Neurons. Neuron. 2012;74:858–873.
10. Beier KT, Gao XJ, Xie S, DeLoach KE, Malenka RC, Luo L. Topological Organization of Ventral Tegmental Area Connectivity Revealed by Viral-Genetic Dissection of Input-Output Relations. Cell Rep. 2019;26:159-167.e6.
11. Cardozo Pinto DF, Yang H, Pollak Dorocic I, de Jong JW, Han VJ, Peck JR, et al. Characterization of transgenic mouse models targeting neuromodulatory systems reveals organizational principles of the dorsal raphe. Nat Commun. 2019;10.
12. Faget L, Osakada F, Duan J, Ressler R, Johnson AB, Proudfoot JA, et al. Afferent Inputs to Neurotransmitter-Defined Cell Types in the Ventral Tegmental Area. Cell Rep. 2016;15:2796–2808.
13. Kalivas PW, Volkow ND. The neural basis of addiction: a pathology of motivation and choice. Am J Psychiatry. 2005;162:1403–1413.
14. Hyman SE, Malenka RC, Nestler EJ. Neural mechanisms of addiction: the role of reward-related learning and memory. Annu Rev Neurosci. 2006;29:565–598.
15. Beier KT, Kim CK, Hoerbelt P, Hung LW, Heifets BD, Deloach KE, et al. Rabies screen reveals GPe control of cocaine-triggered plasticity. Nature. 2017;549:345–350.
16. Tian G, Hui M, Macchia D, Derdeyn P, Rogers A, Hubbard E, et al. An extended Amygdal-midbrain circuit controlling cocaine withdrawal-induced anxiety and reinstatement. Cell Rep. 2022;39:1–16.
17. Juarez B, Han MH. Diversity of Dopaminergic Neural Circuits in Response to Drug Exposure. Neuropsychopharmacology. 2016;41:2424–2446.
18. Mahler S V, Brodnik ZD, Cox BM, Buchta WC, Bentzley BS, Quintanilla J, et al. Chemogenetic Manipulations of Ventral Tegmental Area Dopamine Neurons Reveal Multifaceted Roles in Cocaine Abuse. J Neurosci. 2019;39:503–518.
19. Saal D, Dong Y, Bonci A, Malenka RC. Drugs of abuse and stress trigger a common synaptic adaptation in dopamine neurons. Neuron. 2003;37:577–582.
20. Ungless MA, Whistler JL, Malenka RC, Bonci A. Single cocaine exposure in vivo induces long-term potentiation in dopamine neurons. Nature. 2001;411:583-7.
21. Niehaus JL, Murali M, Kauer JA. Drugs of abuse and stress impair LTP at inhibitory synapses in the ventral tegmental area. Eur J Neurosci. 2010;32:108–117.
22. Bocklisch C, Pascoli V, Wong JCY, House DRC, Yvon C, Roo M De, et al. Cocaine Disinhibits

Dopamine Neurons by Potentiation of GABA Transmission in the Ventral Tegmental Area. Science (80-). 2013;341:1521–1525.

23. Dong Y, Saal D, Thomas M, Faust R, Bonci A, Robinson T, et al. Cocaine-induced potentiation of synaptic strength in dopamine neurons: behavioral correlates in GluRA(-/-) mice. Proc Natl Acad Sci U S A. 2004;101:14282–14287.
24. Creed M, Kaufling J, Fois GR, Jalabert M, Yuan T, Lüscher C, et al. Cocaine exposure enhances the activity of ventral tegmental area dopamine neurons via calcium-impermeable NMDARs. J Neurosci. 2016;36:10759–10768.
25. Backman CM, Malik N, Zhang Y, Shan L, Grinberg A, Hoffer BJ, et al. Characterization of a mouse strain expressing Cre recombinase from the 3' untranslated region of the dopamine transporter locus. Genesis. 2006;44:383–390.
26. Taniguchi H, He M, Wu P, Kim S, Paik R, Sugino K, et al. A Resource of Cre Driver Lines for Genetic Targeting of GABAergic Neurons in Cerebral Cortex. Neuron. 2011;71:995–1013.
27. Vong L, Ye C, Yang Z, Choi B, Chua S, Lowell BB. Leptin Action on GABAergic Neurons Prevents Obesity and Reduces Inhibitory Tone to POMC Neurons. Neuron. 2011;71:142–154.
28. Pedregosa F, Michel V, Grise O, Blondel M, Prettenhofer P, Weiss R, et al. Scikit-learn: Machine Learning in Python. J Mach Learn Res. 2011;12:2825–2830.
29. McInnes L, Healy J, Melville J. UMAP: Uniform Manifold Approximation and Projection for Dimension Reduction. ArXiv. 2018;1802.03426:1–51.
30. Derdeyn P, Hui M, Macchia D, Beier K. Uncovering the Connectivity Logic of the Ventral Tegmental Area. Front Neural Circuits. 2022;15:799688.
31. Waskom M. Seaborn: Statistical Data Visualization. J Open Source Softw. 2021;6:3021.
32. Hunter JD. Matplotlib: a 2D graphics environment. Comput Sci Eng. 2007;9:90–95.
33. Oh SW, Harris JA, Ng L, Winslow B, Cain N, Mihalas S, et al. A mesoscale connectome of the mouse brain. Nature. 2014;508:207–214.
34. Blondel VD, Guillaume JL, Lambiotte R, Lefebvre E. Fast unfolding of communities in large networks. J Stat Mech Theory Exp. 2008;2008.
35. Lein ES, Hawrylycz MJ, Ao N, Ayres M, Bensinger A, Bernard A, et al. Genome-wide atlas of gene expression in the adult mouse brain. Nature. 2007;445:168–176.
36. Brynildsen JK, Mace KD, Cornblath EJ, Weidler C, Pasqualetti F, Bassett DS, et al. Gene coexpression patterns predict opiate-induced brain-state transitions. Proc Natl Acad Sci U S A. 2020;117:19556–19565.
37. Fulcher BD, Murray JD, Zerbi V, Wang XJ. Multimodal gradients across mouse cortex. Proc

Natl Acad Sci U S A. 2019;116:4689–4695.
38. Xie Z, Bailey A, Kuleshov M V., Clarke DJB, Evangelista JE, Jenkins SL, et al. Gene Set Knowledge Discovery with Enrichr. Curr Protoc. 2021;1:1–51.
39. Ji X, Zhang H, Cui Q. A Panel of Synapse-Related Genes as a Biomarker for Gliomas. Front Neurosci. 2020;14:1–8.
40. Wang R, Gurguis CI, Gu W, Ko EA, Lim I, Bang H, et al. Ion channel gene expression predicts survival in glioma patients. Sci Rep. 2015;5:1–10.
41. Berchtold NC, Coleman PD, Cribbs DH, Rogers J, Gillen DL, Cotman CW. Synaptic genes are extensively downregulated across multiple brain regions in normal human aging and Alzheimer's disease. Neurobiol Aging. 2013;34:1653–1661.
42. Shi L, Wang Y, Li C, Zhang K, Du Q, Zhao M. AddictGene: An integrated knowledge base for differentially expressed genes associated with addictive substance. Comput Struct Biotechnol J. 2021;19:2416–2422.
43. Saheki Y, De Camilli P. Synaptic vesicle endocytosis. Cold Spring Harb Perspect Biol. 2012;4.
44. Harding SD, Armstrong JF, Faccenda E, Southan C, Alexander SPH, Davenport AP, et al. The IUPHAR/BPS guide to PHARMACOLOGY in 2022: Curating pharmacology for COVID-19, malaria and antibacterials. Nucleic Acids Res. 2022;50:D1282–D1294.
45. Yamaguchi T, Wang HL, Li X, Ng TH, Morales M. Mesocorticolimbic glutamatergic pathway. J Neurosci. 2011;31:8476–8490.
46. Yamaguchi T, Sheen W, Morales M. Glutamatergic neurons are present in the rat ventral tegmental area. Eur J Neurosci. 2007;25:106–118.
47. Root DH, Mejias-Aponte CA, Zhang S, Wang HL, Hoffman AF, Lupica CR, et al. Single rodent mesohabenular axons release glutamate and GABA. Nat Neurosci. 2014;17:1543–1551.
48. Morales M, Margolis EB. Ventral tegmental area: Cellular heterogeneity, connectivity and behaviour. Nat Rev Neurosci. 2017;18:73–85.
49. Hnasko TS, Hjelmstad GO, Fields HL, Edwards RH. Ventral tegmental area glutamate neurons: electrophysiological properties and projections. J Neurosci. 2012;32:15076–15085.
50. Kim JI, Ganesan S, Luo SX, Wu YW, Park E, Huang EJ, et al. Aldehyde dehydrogenase 1a1 mediates a GABA synthesis pathway in midbrain dopaminergic neurons. Science (80-). 2015;350:102–106.
51. Tritsch NX, Ding JB, Sabatini BL. Dopaminergic neurons inhibit striatal output through non-canonical release of GABA. Nature. 2012;490:262–266.
52. Koob GF. A Role for Brain Stress Systems in Addiction. Neuron. 2008;59:11–34.
53. Koob GF. Brain stress systems in the amygdala and addiction. Brain Res. 2009;1293:61–75.

54. Tian G, Hui M, Macchia D, Derdeyn P, Rogers A, Hubbard E, et al. An extended Amygdal-midbrain circuit controlling cocaine withdrawal-induced anxiety and reinstatement. Cell Rep. 2022;39:1–16.
55. Lammel S, Hetzel A, Häckel O, Jones I, Liss B, Roeper J. Unique Properties of Mesoprefrontal Neurons within a Dual Mesocorticolimbic Dopamine System. Neuron. 2008;57:760–773.
56. Sian J, Youdim M, Riederer, P et al. Biochemical Anatomy of the Basal Ganglia and Associated Neural Systems. In: Siegel G, Agranoff B, Albers, RW et al., editors. Basic Neurochem. Mol. Cell. Med. Asp., . 6th ed.1999.
57. Lanciego JL, Luquin N, Obeso JA. Functional neuroanatomy of the basal ganglia. Cold Spring Harb Perspect Med. 2012;2:1–20.
58. Li H, Eid M, Pullmann D, Chao YS, Thomas AA, Jhou TC. Entopeduncular nucleus projections to the lateral habenula contribute to cocaine avoidance. J Neurosci. 2021;41:298–306.
59. López AJ, Jia Y, White AO, Kwapis JL, Espinoza M, Hwang P, et al. Medial habenula cholinergic signaling regulates cocaine-associated relapse-like behavior. Addict Biol. 2019;24:403–413.
60. Tan D, Nuno-Perez A, Mameli M, Meye FJ. Cocaine withdrawal reduces GABABR transmission at entopeduncular nucleus – lateral habenula synapses. Eur J Neurosci. 2019;50:2124–2133.
61. Koob GF, Volkow ND. Neurocircuitry of addiction. Neuropsychopharmacology. 2010;35:217–238.
62. Liu Y, Lin D, Wu B, Zhou W. Ketamine abuse potential and use disorder. Brain Res Bull. 2016;126:68–73.
63. Ni A, Lee Cantrell F, Clark RF. Ketamine exposure demographics and outcomes over 16 years as reported to US poison centers. Am J Emerg Med. 2018;36:1459–1462.
64. Dillon P, Copeland J, Jansen K. Patterns of use and harms associated with non-medical ketamine use. Drug Alcohol Depend. 2003;69:23–28.
65. Morgan CJA, Curran HV. Ketamine use: A review. Addiction. 2012;107:27–38.
66. Ryder S, Way WL, Trevor AJ. Comparative pharmacology of the optical isomers of ketamine in mice. Eur J Pharmacol. 1978;49:15–23.
67. Finck AD, Ngai SH. Opiate receptor mediation of ketamine analgesia. Anesth Analg. 1982;56:291–297.
68. Hustveit O, Maurset A, Oye I. Interaction of the Chiral Forms of Ketamine with Opioid,

Phencyclidine, c and Muscarinic Receptors. Pharmacol Toxicol. 1995;77:355–359.

69. Bonaventura J, Lam S, Carlton M, Boehm MA, Gomez JL, Solís O, et al. Pharmacological and behavioral divergence of ketamine enantiomers:implications for abuse liability. Mol Psychiatry. 2021;26:6704–6722.
70. Williams NR, Heifets BD, Bentzley BS, Blasey C, Sudheimer KD, Hawkins J, et al. Attenuation of antidepressant and antisuicidal effects of ketamine by opioid receptor antagonism. Mol Psychiatry. 2019;24:1779–1786.
71. Williams NR, Heifets BD, Blasey C, Sudheimer K, Pannu J, Pankow H, et al. Attenuation of antidepressant effects of ketamine by opioid receptor antagonism. Am J Psychiatry. 2018;175:1205–1215.
72. Gelernter J, Kranzler HR, Sherva R, Koesterer R, Almasy L, Zhao H, et al. Genome-wide association study of opioid dependence: Multiple associations mapped to calcium and potassium pathways. Biol Psychiatry. 2014;76:66–74.
73. Malcolm R, Brady KT, Moore J, Kajdasz D. Amlodipine treatment of cocaine dependence. J Psychoactive Drugs. 1999;31:117–120.
74. Altamura AC, Regazzetti MG, Porta M. Nimodipine in human alcohol withdrawal syndrome - an open study. Eur Neuropsychopharmacol. 1990;1:37–40.
75. Rosse R, Alim T, Fay-McCarthy M, Collins J, Vocci F, Lindquist T, et al. Nimodipine Pharmacotherapeutic Adjuvant Therapy for Inpatient Treatment of Cocaine Dependence. Clin Neuropharmacol. 1994;17:348–358.
76. Muntaner C, Kumor K, Nagoshi C, Jaffe J. Effect of nifedipine pretreatment on subjective and cardiovascular responses to intravenous cocaine in humans. Drug Alcohol Depend. 1991;105:37–41.
77. Johnson BA, Roache JD, Ait-Daoud N, Wells LT, Mauldin JB, Cormier RH. Effects of Isradipine on Cocaine-Induced Subjective Mood. J Clin Psychopharmacol. 2004;24:180–191.
78. Vaupel DB, Lange WR, London ED. Effects of verapamil on morphine-induced euphoria, analgesia and respiratory depression in humans. J Pharmacol Exp Ther. 1993;267:1386–1394.

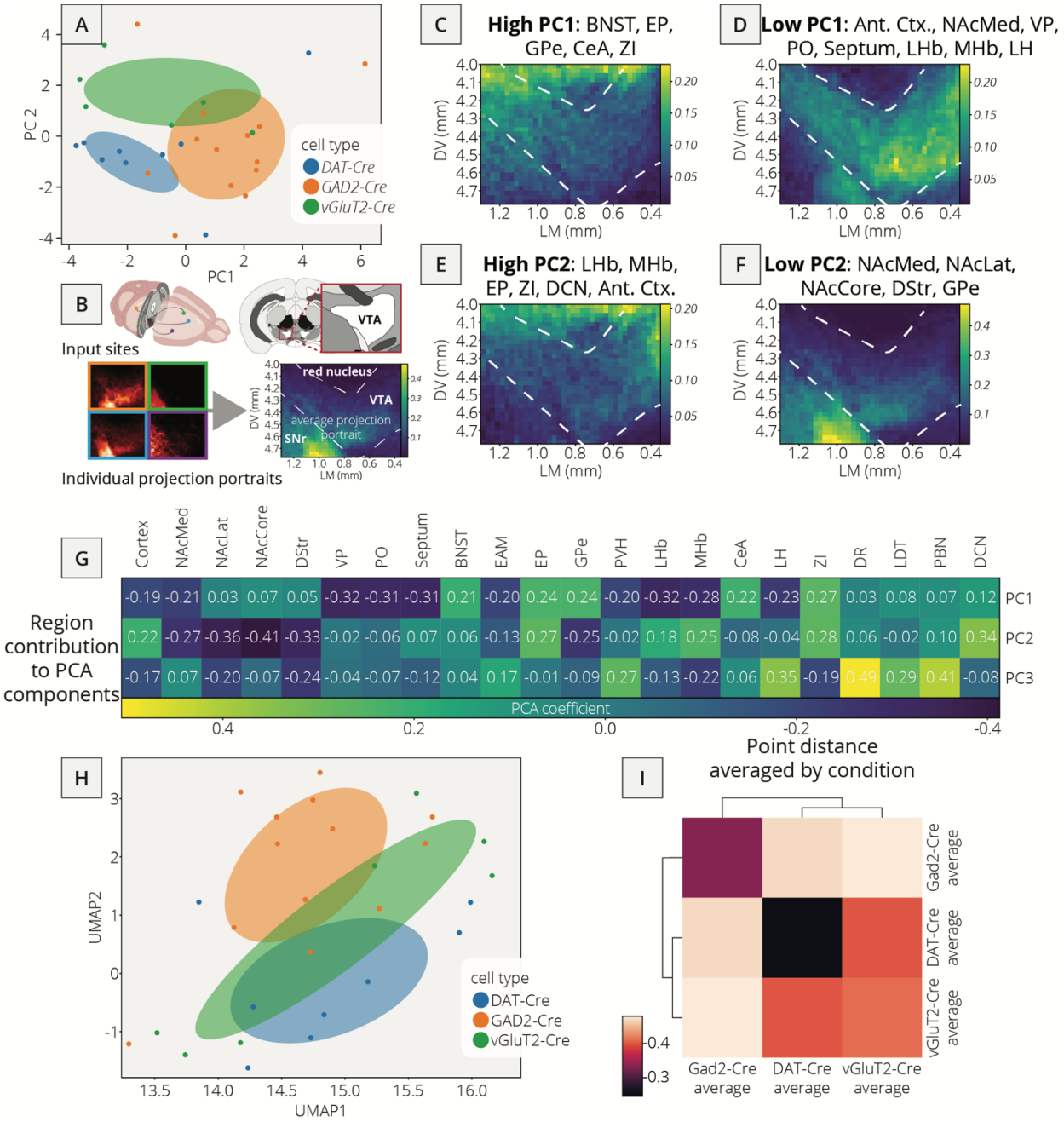

Figure 1: Dimensionality reduction of RABV input tracing to 3 different VTA cell types.

(A) PCA of input labeling from DAT-Cre, GAD2-Cre, and vGlut2-Cre brains. For this and other figures, ellipsoids were centered at the average coordinate of a condition and stretched one standard deviation along the primary and secondary axes.

(B) Schematic of how projection portraits are constructed. A representative slice of the VTA is considered for experiments from the Allen Mouse Brain Connectivity Atlas with injections into relevant brain regions that provide input to the VTA. Projection density values in this slice are averaged and visualized to obtain the projection portrait in the VTA for that group of regions.

(C) Projection portrait of the VTA based on inputs from regions with a high positive contribution to PC1: BNST, EP, GPe, CeA, and ZI.

(D) Projection portrait of the VTA based on inputs from regions with a large negative contribution to PC1: anterior cortex, NAcMed, VP, PO, septum, LHb, MHb, and LH.

(E) Projection portrait of the VTA based on inputs from regions with a high positive contribution to PC2: LHb, MHb, EP, ZI, DCN, and anterior cortex.

(F) Projection portrait of the VTA based on inputs from regions with a large negative contribution to PC2: NAcMed, NAcLat, NAcCore, DStr, and GPe.

(G) Heatmap of the contributions of each brain region, or feature, in the data to PCs 1 through 3.

(H) UMAP embedding of input labeling from DAT-Cre, GAD2-Cre, and vGlut2-Cre brains.

(I) Correlogram generated using the average Euclidean distance of data points from each other from 20 UMAP embeddings.

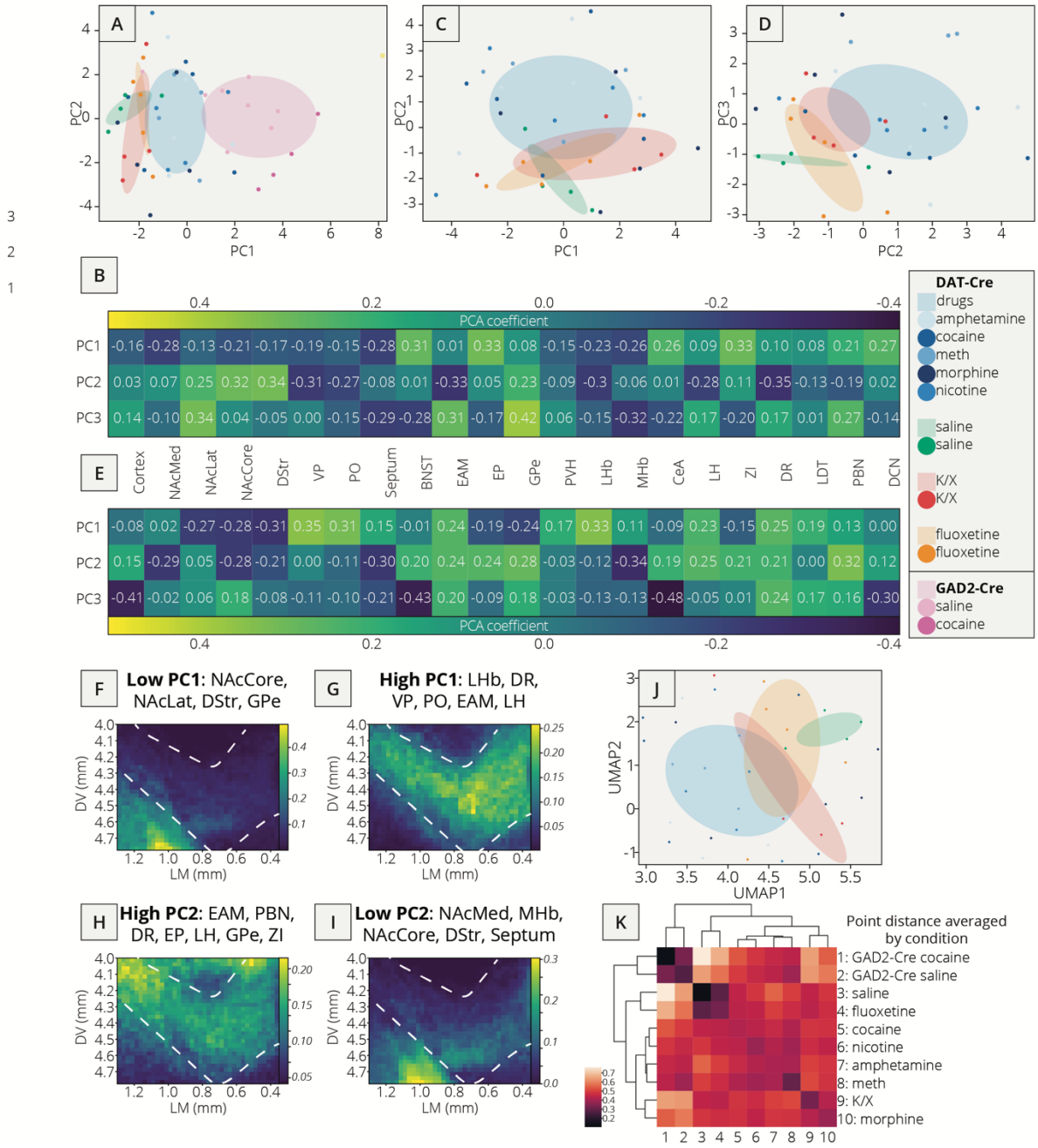

Figure 2: Dimensionality reduction analysis of brains from animals treated with a single exposure to a drug.

(A) PC1 and PC2 of DAT-Cre and GAD2-Cre brains. DAT-Cre mice were anesthetized with ketamine/xylazine and treated with saline or anesthetized with isoflurane and treated with saline or one of drugs amphetamine, cocaine, meth, morphine, or nicotine, or fluoxetine. GAD2-Cre mice were anesthetized with isoflurane and treated with saline or cocaine.

(B) Heatmap of the contributions of each brain region in the dataset from panel A to PC1 through PC3.

(C) PC1 and PC2 of brains from DAT-Cre mice anesthetized with isoflurane and treated with amphetamine, cocaine, meth, morphine, nicotine, fluoxetine, or saline, or anesthetized with ketamine/xylazine and treated with saline.

(D) PC2 and PC3 of the same group of brains as shown in panel C.

(E) Heatmap of the contributions of each brain region to PC1 through PC3 for data shown in panels C and D.

(F) Projection portrait of the VTA based on inputs from regions with a large negative contribution to PC1, based on data from panel C-E: NAcCore, NAcLat, DStr, GPe.

(G) Projection portrait based on inputs from regions with a high positive contribution to PC1, based on data from panels C-E: LHb, DR, VP, PO, EAM, LH.

(H) Projection portrait based on inputs from regions with a high positive contribution to PC2, based on data from panels C-E: EAM, PBN, DR, EP, LH, GPe, ZI.

(I) Projection portrait based on inputs from regions with a large negative contribution to PC2, based on data from panels C-E: NAcMed, NAcCore, DStr, Septum, MHb.

(J) UMAP embedding of data from the brains of DAT-Cre mice anesthetized with isoflurane and treated with amphetamine, cocaine, meth, morphine, nicotine, fluoxetine, or saline, or anesthetized with ketamine/xylazine and treated with saline.

(K) Correlogram showing average Euclidean distance of data points over 20 UMAP embeddings of the data presented in panel J.

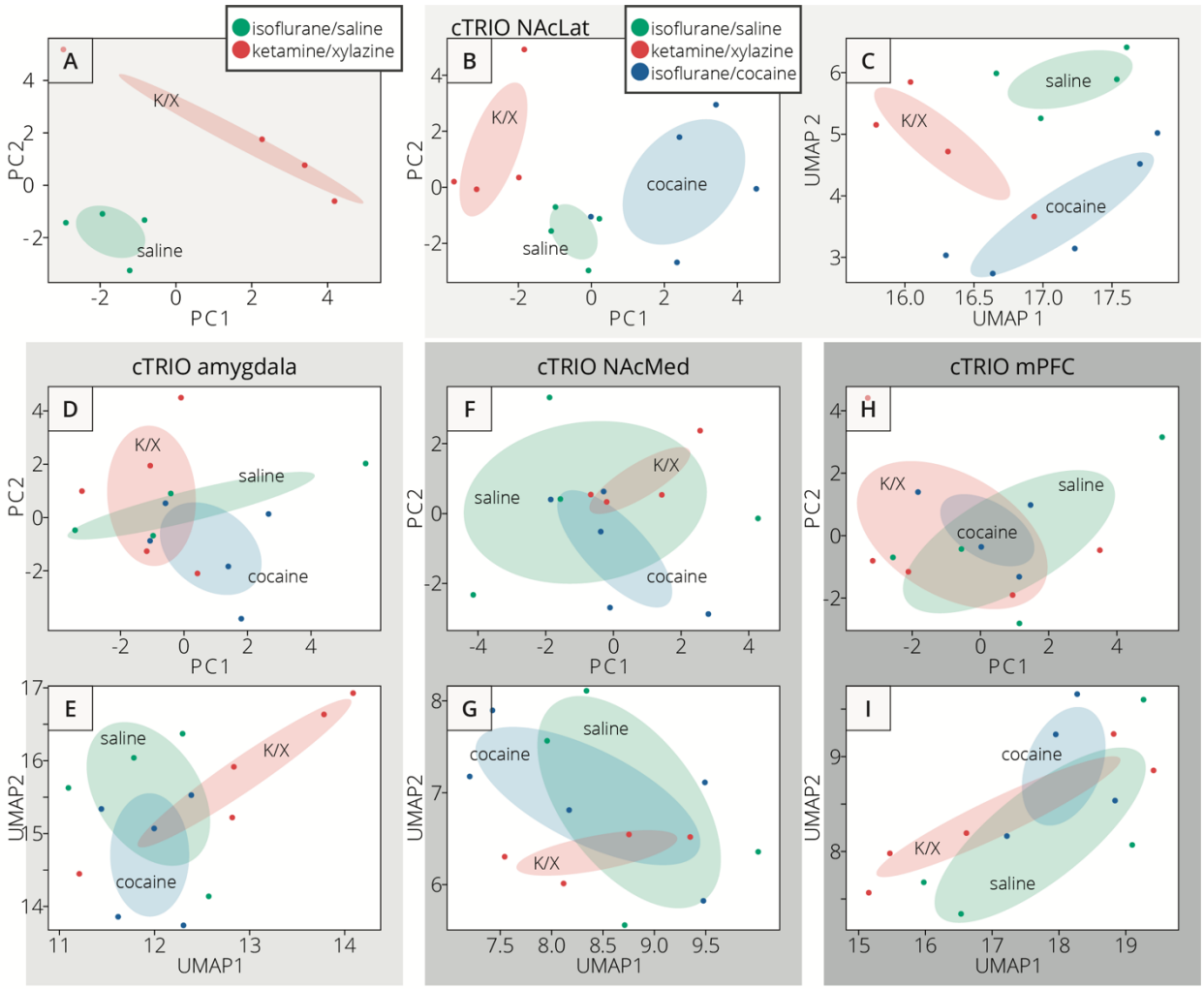
A
isoflurane/saline
ketamine/xylazine
K/X
saline
PC2
PC1
cTRIO NAcLat
B
isoflurane/saline
ketamine/xylazine
isoflurane/cocaine
K/X
cocaine
saline
C
saline
K/X
cocaine
UMAP 2
UMAP 1
cTRIO amygdala
D
K/X
saline
cocaine
E
saline
K/X
cocaine
UMAP2
UMAP1
cTRIO NAcMed
F
K/X
saline
cocaine
G
saline
cocaine
K/X
cTRIO mPFC
H
K/X
saline
cocaine
I
cocaine
K/X
saline

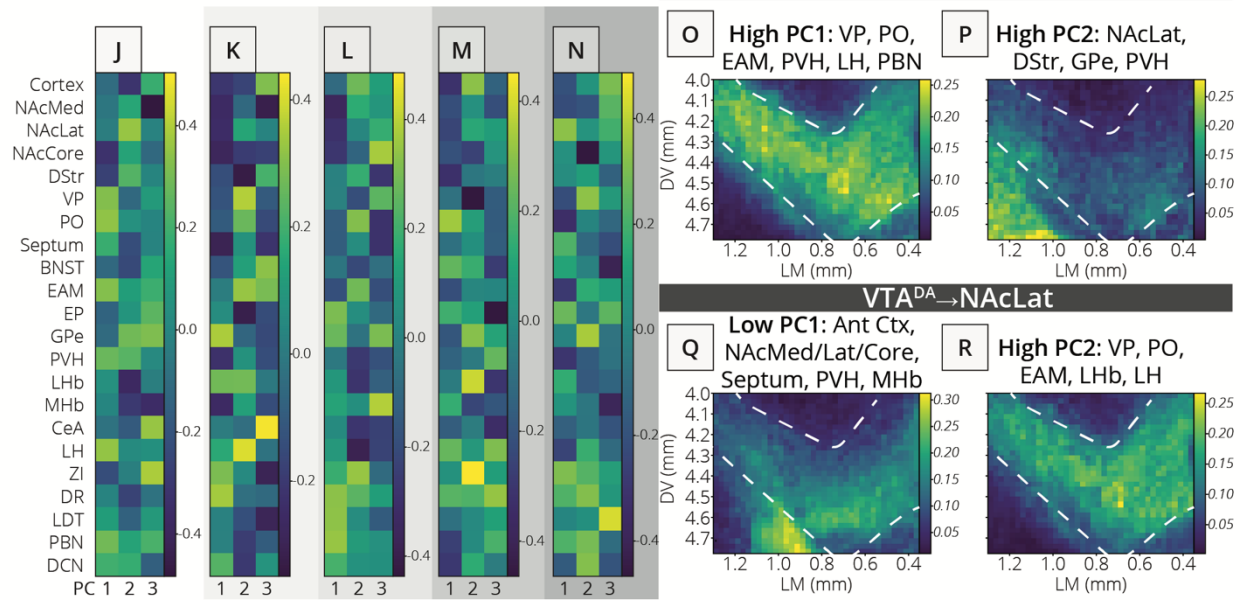
J
K
L
M
N
Cortex
NAcMed
NAcLat
NAcCore
DStr
VP
PO
Septum
BNST
EAM
EP
GPe
PVH
LHb
MHb
CeA
LH
ZI
DR
LDT
PBN
DCN
PC 1 2 3
All DA cells
O
High PC1: VP, PO, EAM, PVH, LH, PBN
P
High PC2: NAcLat, DStr, GPe, PVH
DV (mm)
LM (mm)
VTA^DA→NAcLat
Q
Low PC1: Ant Ctx, NAcMed/Lat/Core, Septum, PVH, MHb
R
High PC2: VP, PO, EAM, LHb, LH

Figure 3: Dimensionality reduction analysis of brains from animals anesthetized with isoflurane and treated with either cocaine or saline, or anesthetized with ketamine/xylazine and treated with saline.

(A) PCA plot of isoflurane-anesthetized and K/X-anesthetized mice.

(B) PCA plot of RABV input mapping experiments to VTA^{DA}→NAcLat cells.

(C) UMAP plot of input mapping experiments to VTA^{DA}→NAcLat cells.

(D) PCA plot of input mapping experiments to VTA^{DA}→amygdala cells.

(E) UMAP plot of input mapping experiments to VTA^{DA}→amygdala cells.

(F) PCA plot of input mapping experiments to VTA^{DA}→NAcMed cells.

(G) UMAP plot of input mapping experiments to VTA^{DA}→NAcMed cells.

(H) PCA plot of input mapping experiments to VTA^{DA}→mPFC cells.

(I) UMAP plot of input mapping experiments to VTA^{DA}→mPFC cells.

(J-N) Heatmap of the contributions of each brain region to PC1 to PC3 for data shown in (J) panel A, (K) panel B, (L) panel D, (M) panel F, (N) panel H.

(O) Projection portrait of regions with high PC1 contributions in all VTA^{DA} cells: VP, PO, EAM, PVH, LH, PBN.

(P) Projection portrait of regions with high PC2 contributions in VTA^{DA} cells: NAcLat, DStr, GPe, PVH.

(Q) Projection portrait of regions with low PC1 contributions in VTA^{DA}→NAcLat cells: cortex, NAcMed, NAcLat, NacCore, septum, PVH, MHb.

(R) Projection portrait of regions with high PC2 contributions in VTA^{DA}→NAcLat cells: VP, PO, EAM, LHb, LH.

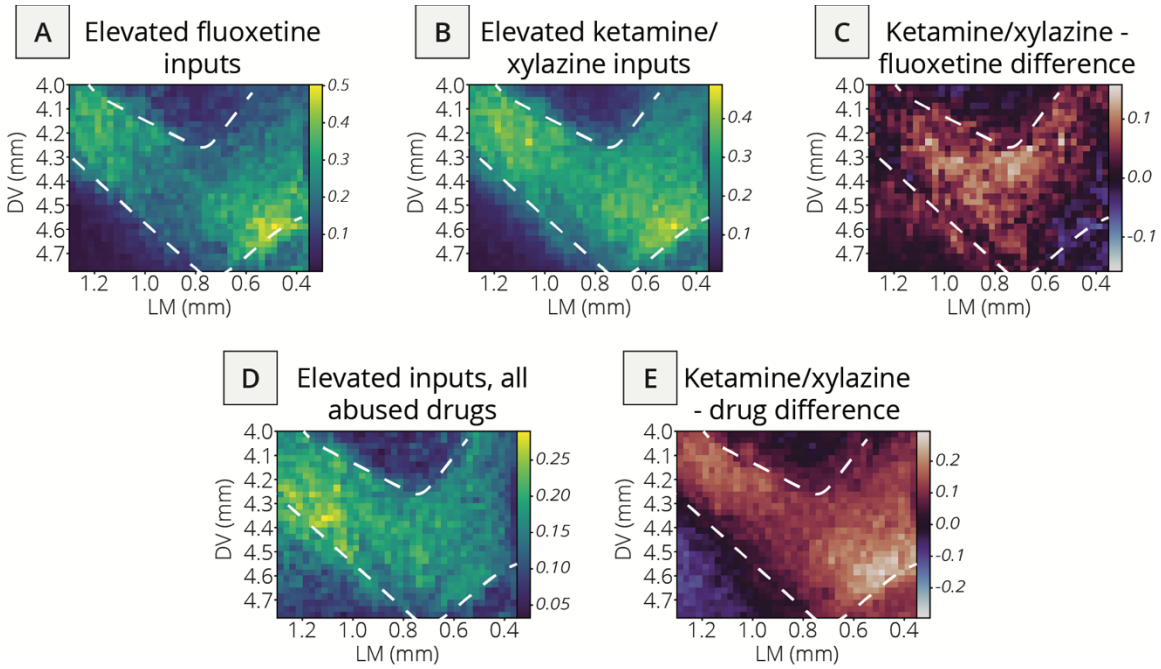

Figure 4: Projection portraits of the VTA highlighting regions with elevated or depressed RABV labeling in experimental mice.

(A) Projection portrait of regions with elevated RABV input labeling in fluoxetine-treated mice relative to saline-treated mice: DCN, LH, PVH.

(B) Projection portrait of inputs elevated by K/X anesthesia relative to isoflurane anesthesia: DCN, EAM, LH, PBN, PO, PVH.

(C) Difference in the projection portraits shown in panels A and B to compare portraits generated using K/X anesthesia and saline, and isoflurane anesthesia and fluoxetine.

(D) Projection portrait of inputs elevated by an average of all drugs of abuse (amphetamine, cocaine, meth, morphine, nicotine): BNST, GPi, GPe, CeA, LH, ZI, DR, PBN, DCN.

(E) Difference in inputs from panels B and D to compare K/X to addictive drug groups.

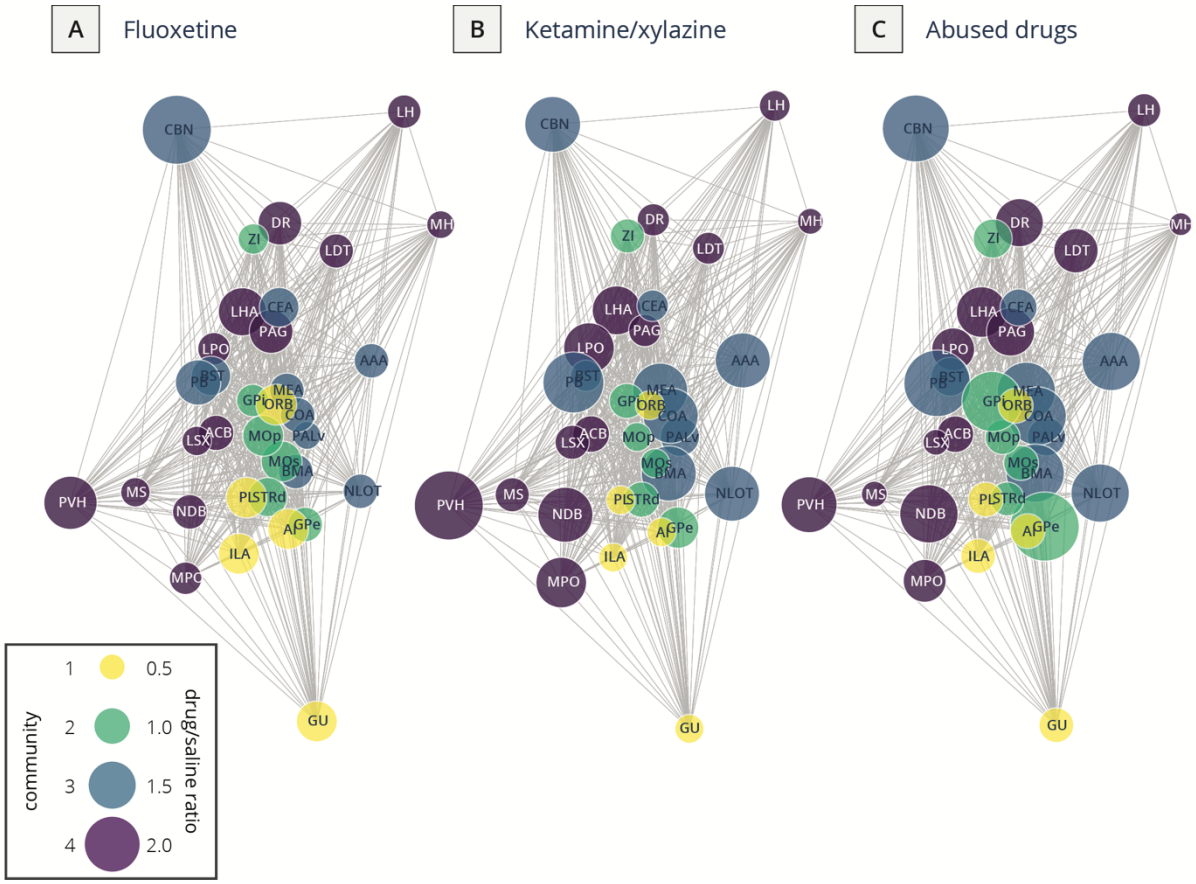

Figure 5: Network connectivity matrix of quantified input brain regions in RABV mapping data. Anatomical connectivity is based off of data from the Allen Mouse Brain Connectivity Atlas. Node size is determined by the ratio of RABV-labeled inputs in experimental vs. the isoflurane/saline condition. Node color represents the identity of the community into which each region was assigned.

(A) Relative connectivity matrix of fluoxetine vs. saline-treated mice, both anesthetized with isoflurane.

(B) Relative connectivity matrix of K/X-anesthetized vs. isoflurane-anesthetized mice.

(C) Relative connectivity matrix for the average of the addictive drugs vs. saline-treated mice, all anesthetized using isoflurane.

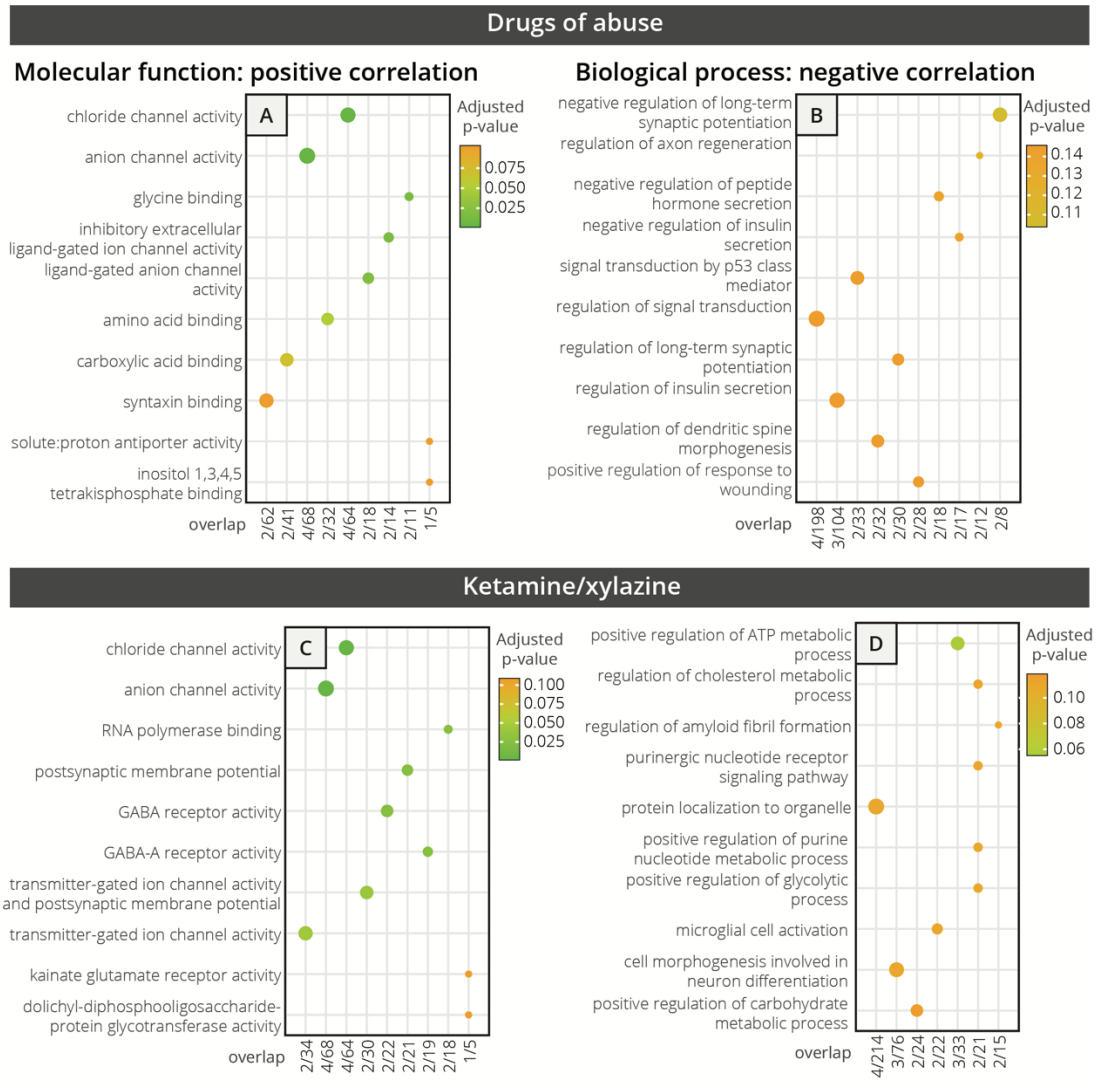

Figure 6: Gene ontology analysis of top 50 genes correlated to differences in RABV input labeling obtained from experimental vs. control mice.

(A-B) GO from an average of the addictive drug conditions vs. saline-treated controls, all anesthetized using isoflurane.

(C-D) GO from K/X-anesthetized relative to isoflurane-anesthetized mice. Panels A and C show molecular function-related gene classes whose expression was positively correlated with RABV labeling differences, and panels B and D show GO analyses that reflect biological process-related gene classes whose expression was negatively correlated with RABV labeling differences.

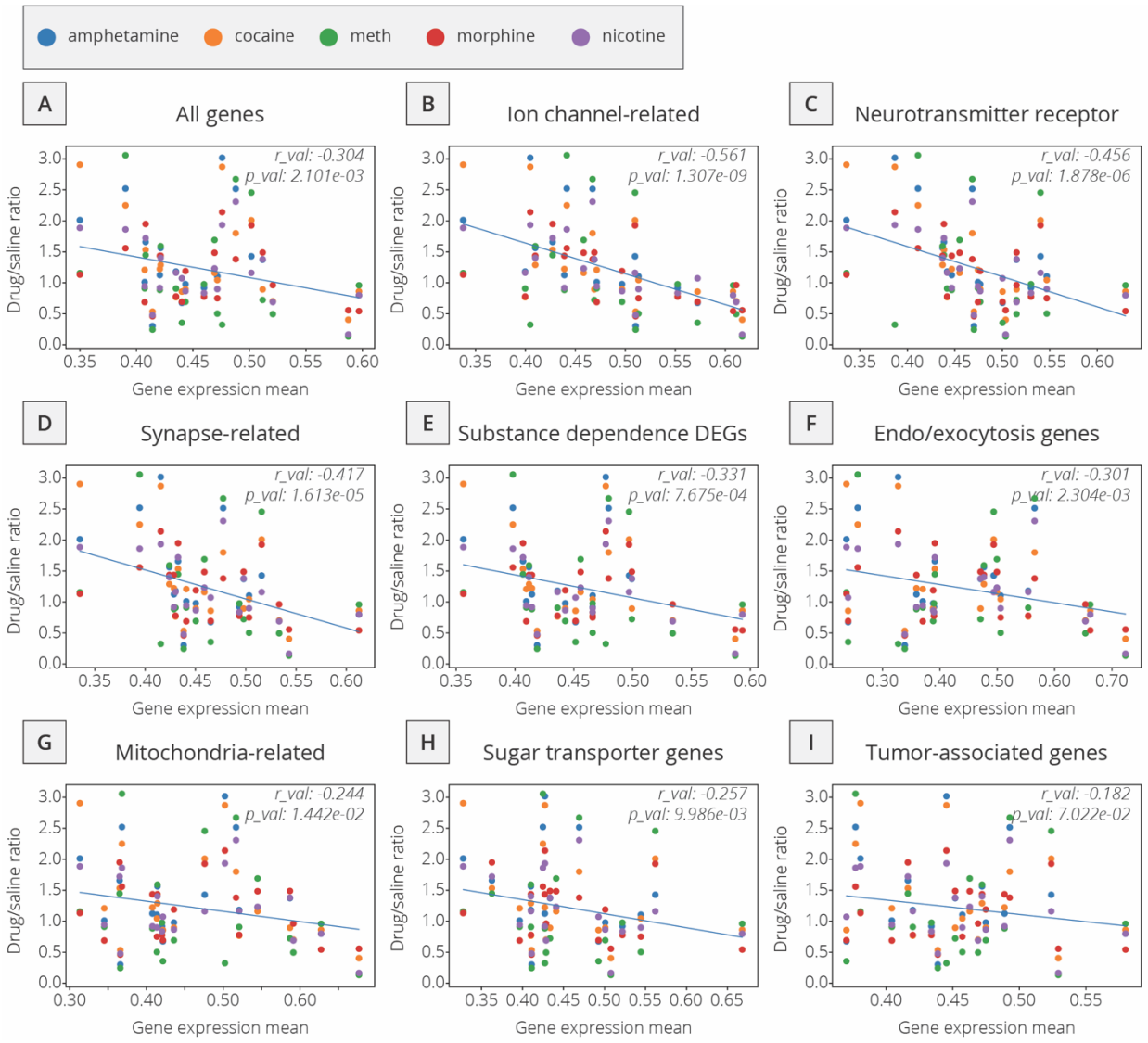

Figure 7: Relationship between relative RABV labeling in addictive drug/saline-treated groups and mean basal gene expression of all genes or gene subgroups. Linear regressions are shown for all five examined drugs against different gene classes, including (A) all genes, (B) ion channel-related genes, (C) neurotransmitter-related genes, (D) synapse-related genes, (E) DEGs related to substance abuse, (F) endo- and exocytosis-related genes, (G) mitochondria-related genes, (H) sugar transporter genes, and (I) tumor-associated genes.

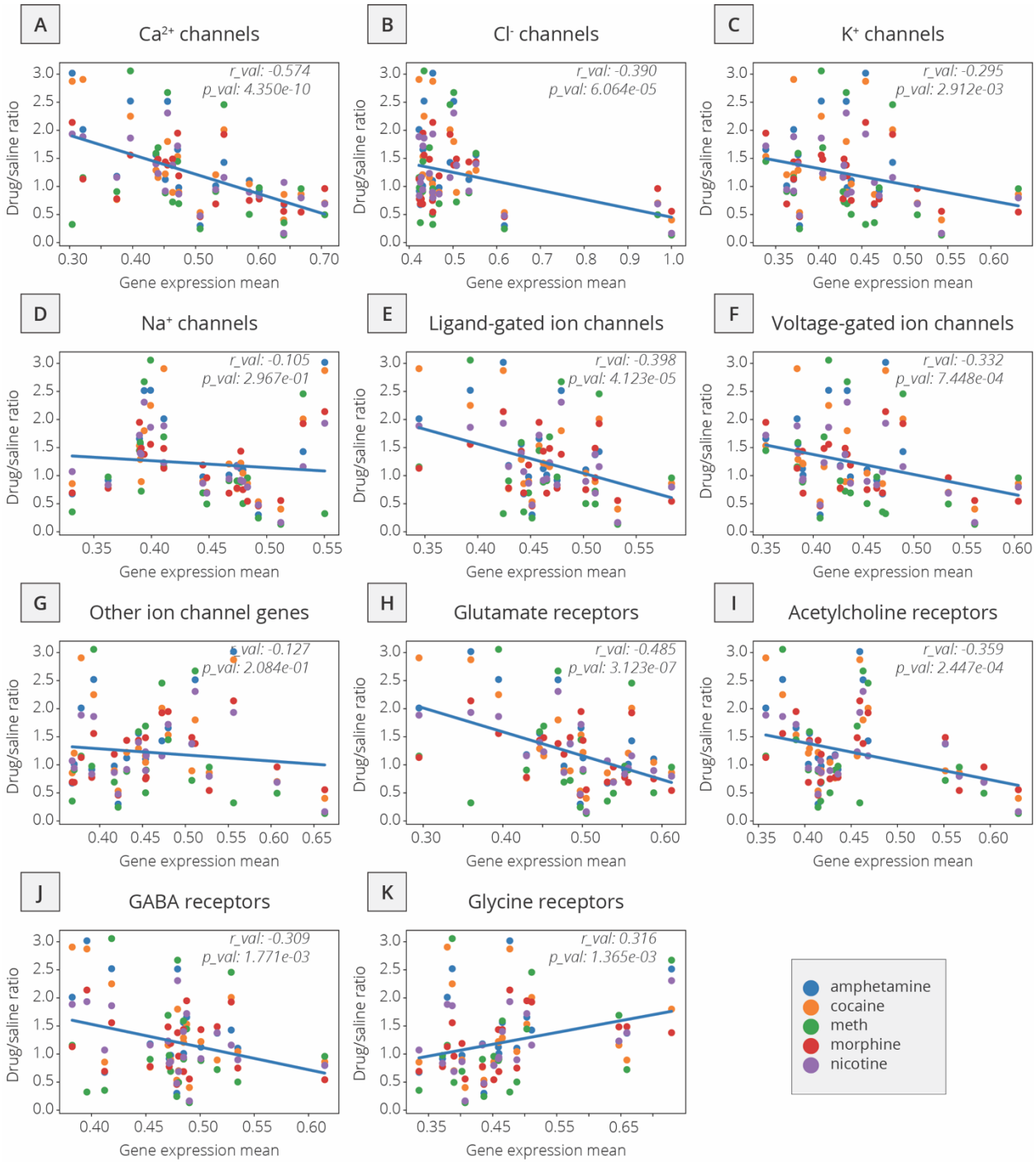

Figure 8: Relationship between relative RABV labeling in addictive drug/saline-treated groups and mean basal gene expression of subtypes of ion channels and neurotransmitter receptors. Linear regressions are shown for all five examined drugs against different gene classes, including (A) Ca^{2+} channels, (B) Cl^{-} channels, (C) K^{+} channels, (D) Na^{+} channels, (E) ligand-gated ion channels, (F) voltage-gated ion channels, (G) other ion channels, (H) glutamate receptors, (I) acetylcholine receptors, (J) GABA receptors, (K) glycine receptors.